

We then investigate how the strain energy of the MITC3-HR shell finite element varies according to the rotation angle ( $\theta$ ) of the contravariant base vector in the in-plane twisting mode. Note that the in-plane twisting mode results in only non-zero transverse shear strains. When the single triangular elements shown in Fig. 3.8(a) are twisted at the angle  $\varphi$  about the z-axis located at the barycenter, the in-plane twisting mode shown in Fig. 3.8(b) is obtained:  $\theta_x^1 = \theta_x^3 = \theta_y^1 = \theta_y^2 = 1/\sqrt{12}$  and  $\theta_x^2 = \theta_y^3 = -2/\sqrt{12}$ . We use  $L=1.0$ ,  $E=1.7472 \times 10^7$  and  $\nu=0.3$ . The singledisplacement based 3-node and MITC3 shell finite elements give the exact strain energy in the in-plane twisting mode, which results in only non-zero transverse shear strains.

Fig. 3.9 shows the ratio of the strain energy of the MITC3-HR shell finite element to the strain energy of the MITC3 shell finite element depending on the rotation angle of the contravariant base vector ( $0 \leq \theta \leq 89$  deg) when the in-plane twisting mode is applied. Note that less strain energy stored in the element means that the element is more flexible. The MITC3-HR shell finite element has the same flexibility as the MITC3 shell finite element when the rotation angle  $\theta=0$  deg. However, as the angle increases, the MITC3-HR shell finite element becomes increasingly flexible. As the angle approaches 90 deg, the zero strain energy is calculated when  $\theta=90$  deg. Therefore, it can be expected that the 10th mode of the MITC3-HR shell finite element with  $\theta=89$  deg becomes the spurious in-plane twisting mode when  $\theta=90$  deg.

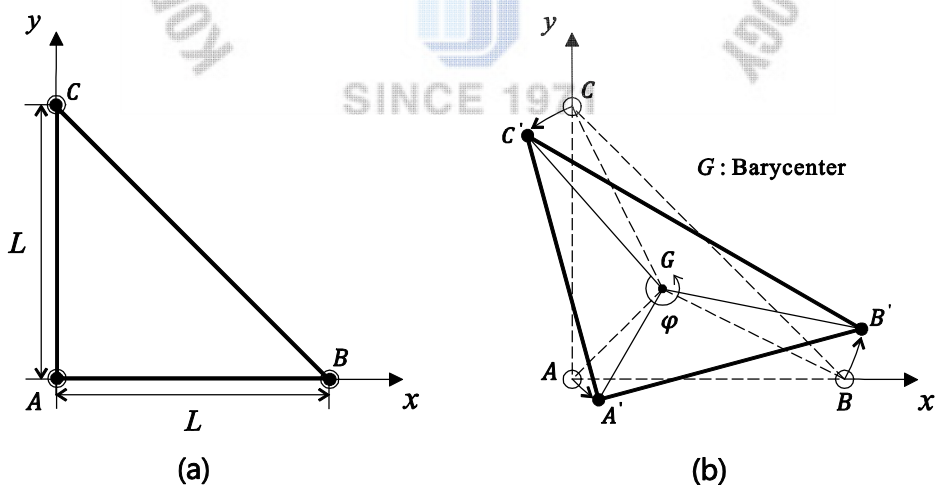


Fig. 3.7 Strain energy mode test ( $L = 1.0$ ,  $E = 1.7472 \times 10^7$  and  $\nu = 0.3$ ). (a) A single triangular shell finite element. (b) In-plane twisting mode for the single shell finite element. The dotted and solid lines correspond to the top surfaces before and after deformation, respectively.

Table 3.2 The eigenvalues of the strain energy modes of the MITC3-HR shell finite element for the plate bending problem shown in Fig. 3.8(a) when  $t/L = 1/1,000$ . Modes 1 to 6 are rigid body modes. Modes 12, 14 and 15 are membrane modes.

Mode	Angle( $\theta$ )				
	0deg (MITC3)	30deg	60deg	89deg	90deg
7	6.6764E-04	6.6764E-04	6.6764E-04	6.6764E-04	6.6764E-04
8	8.1454E-04	8.1454E-04	8.1454E-04	8.1265E-04	1.0752E-03
9	2.4924E-03	2.4924E-03	2.4924E-03	2.4924E-03	2.4924E-03
10	3.6928E+02	2.7702E+02	9.2381E+01	1.1284E-01	0.0000E+00
11	4.6707E+03	4.6696E+03	4.6676E+03	4.6667E+03	4.6667E+03
13	1.1760E+04	1.1760E+04	1.1760E+04	1.1760E+04	1.1760E+04

Table 3.3 The eigenvalues of the strain energy modes of the MITC3-HR shell finite element for the platebending problem shown in Fig. 3.8(a) when  $t/L = 1/10,000$ . Modes 1 to 6 are rigid body modes. Modes 12, 14 and 15 are membrane modes.

Mode	Angle( $\theta$ )				
	0deg (MITC3)	30deg	60deg	89deg	90deg
7	6.6764E-07	6.6764E-07	6.6764E-07	6.6764E-07	6.6764E-07
8	8.1455E-07	8.1455E-07	8.1455E-07	8.1453E-07	1.0752E-06
9	2.4924E-06	2.4924E-06	2.4924E-06	2.4924E-06	2.4924E-06
10	3.6928E+01	2.7702E+01	9.2381E+00	1.1258E-02	0.0000E+00
11	4.6707E+02	4.6696E+02	4.6676E+02	4.6667E+02	4.6667E+02
13	1.1760E+03	1.1760E+03	1.1760E+03	1.1760E+03	1.1760E+03

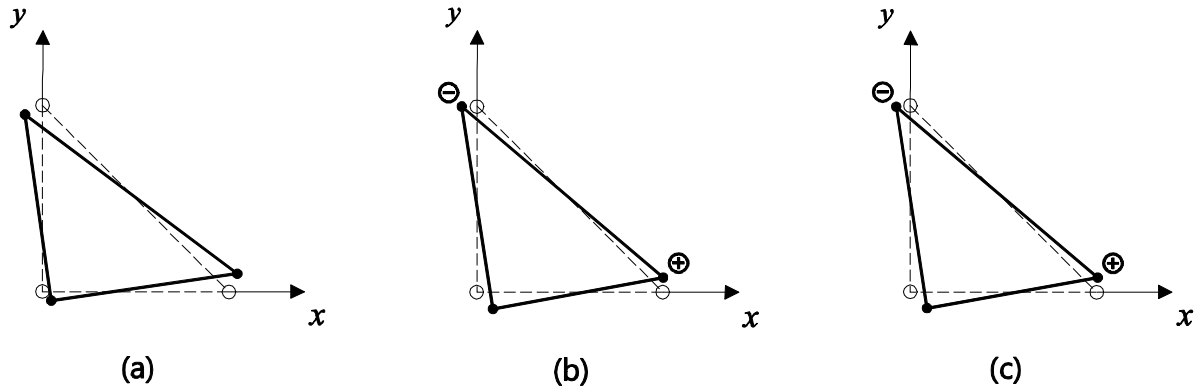


Fig. 3.8 Shapes of the normalized 10th strain energy mode. The dotted and solid lines correspond to the top surfaces before and after deformation, respectively. Plus and minus signs denote small out-of-plane displacements in the  $z$  and  $-z$  directions. (a) Displacement based 3-node shell finite element. (b) MITC3 shell finite element (MITC3-HR shell finite element when  $\theta = 0$  deg). (c) MITC3-HR shell finite element when  $\theta = 89$  deg.

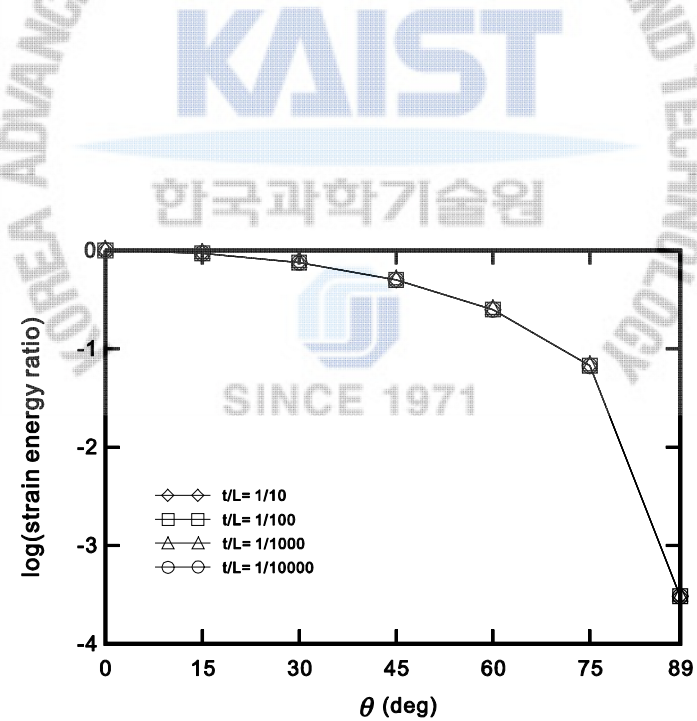


Fig. 3.9 Ratio of the strain energy of the MITC3-HR shell finite element to the strain energy of the MITC3 shell finite element depending on the rotation angle ( $\theta$ ) of the contravariant base vectors in the in-plane twisting mode.

In order to understand why the behaviors of the MITC3-HR shell finite element with  $\theta = 0$  deg are identical to the MITC3 shell finite element and why the MITC3-HR element with  $\theta = 90$  deg has a spurious mode, we calculate the approximated transverse shear strains in Eq.(3.33) for the single triangular element with an uniform thickness (node numbering: 1→2→3) in Fig. 3.7(a) and then separate the covariant transverse shear strain fields corresponding to the original contravariant base vectors  $\vec{g}^j$ ,

$$\begin{aligned}\bar{e}_{rt}^A &= -\alpha_1 \sin \theta + \alpha_2 \cos \theta + \alpha_3 (r \sin \theta + s \cos \theta), \\ \bar{e}_{st}^A &= \alpha_1 \cos \theta + \alpha_2 \sin \theta + \alpha_3 (-r \cos \theta + s \sin \theta).\end{aligned}\quad (3.44)$$

When  $\theta = 0$  deg, Eq. (3.44) has the same form as Eq. (3.13), this results in  $\vec{\gamma}^A = \vec{\gamma}^M$  in Eq. (3.31). In this case, the MITC3-HR shell finite element becomes identical to the MITC3 shell finite element. In the case of  $\theta = 90$  deg, Eq. (3.44) is as follows:

$$\begin{aligned}\bar{e}_{rt}^A &= -\alpha_1 + \alpha_3 r, \\ \bar{e}_{st}^A &= \alpha_2 + \alpha_3 s\end{aligned}\quad (3.45)$$

In addition, a comparison of Eq. (3.45) and Eq. (3.13) shows that the linear terms in each covariant transverse shear strain component are switched. This results in  $\alpha_3 = 0$ ; thus, the constant transverse shear strain field is obtained. As pointed out in the literature [11], the 3-node plate/shell finite elements with a constant transverse shear strain field display a spurious zero energy mode.

Through the studies in this section, we can conclude that the special approximated transverse shear strain field introduced by the modified Hellinger-Reissner functional selectively increases the flexibility of the MITC3 shell finite element corresponding to the 10th strain energy mode. In other words, the transverse shear strains by the 10th strain energy mode that contains both the in-plane twisting and bending modes becomes smaller in the MITC3-HR shell finite element.

In all the following numerical examples, we use the rotation angle of the contravariant base vectors,  $\theta = 89$  deg, to make the MITC3-HR shell finite element flexible enough in the 10th strain energy mode without the spurious energy mode.

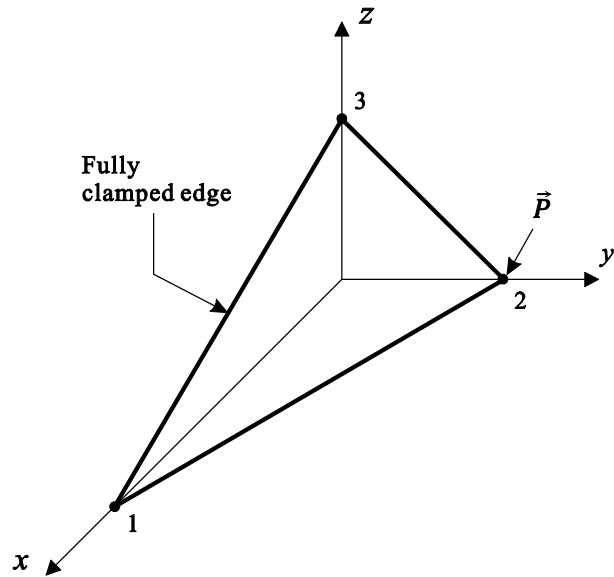


Fig. 3.10 A single 3-node triangular shell finite element for the isotropic test. The input values of the geometry are presented in Table 3.1.  $\vec{P} = [F_x \quad F_y \quad F_z \quad M_\alpha \quad M_\beta]^T$ .

Table 3.4 Input values for the geometry shown in Fig. 3.10 for the isotropic test.

Node( $i$ )	Cartesian coordinate ( $\vec{x}_i$ )			Director vectors ( $V_n^i$ )			Thicknesses
	$x_i$	$y_i$	$z_i$	$V_{nx}^i$	$V_{yx}^i$	$V_{nz}^i$	
1	2.0	0.0	0.0	0.43775	0.87549	0.20467	0.1
2	0.0	1.0	0.0	-0.18273	0.69520	0.69520	0.01
3	0.0	0.0	1.0	0.43775	0.20467	0.87549	0.2

### 3.5.2 Isotropy test

A single 3-node triangular shell finite element in Fig. 3.10 is analyzed with 3 different node numberings. All the input values are the same except for the node numbering. Different sequences of node numberings are used as follows: 1→2→3, 2→3→1 and 3→1→2. The results should be the same for all possible tip forces and

moments. The input values of the geometry of the 3-node triangular shell element are presented in Table 3.3. Each node has different thickness and director vectors, which are not normal to the shell midsurface in order to consider a general case.

The MITC3-HR shell finite element gives identical results regardless of the numbering sequences; that is, the element passes the isotropic element test as the MITC3 shell finite element does. Also, the isotropic behavior is independent of the rotation angle of the contravariant base vectors. Of course, the MITC3-HR element shows isotropic behavior for other arbitrary element geometries.

### 3.5.3 Patch test

The mesh shown in Fig. 3.11 is used to perform the patch test [1]. The minimum number of degrees of freedom is constrained so as to prevent rigid body motions. Nodal forces that should result in constant stress conditions are applied. The constant stress should be calculated to pass the patch test. The MITC3-HR shell finite element passes the membrane, bending, and transverse shearing patch tests.

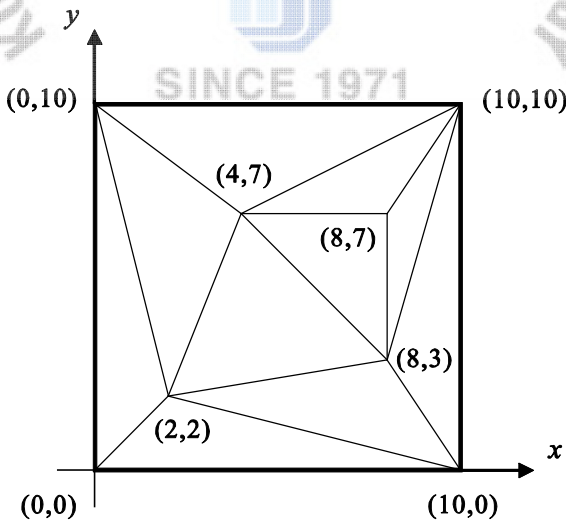


Fig. 3.11 Triangular mesh used for the patch tests.

### 3.6 Convergence studies

In this section, convergence studies using appropriate benchmark problems are performed to study the behavior of shell elements: a clamped square plate problem, a sixty-degree skew plate problem, cylindrical shell problems, and hyperboloid shell problems [1,2,10,40]. These problem solutions pertain to measuring the errors in an appropriate norm considering membrane and bending dominated problems with various shell curvatures, shell thickness values, and boundary conditions.

To measure the error in the finite element solution, we use the s-norm proposed by Hiller and Bathe [41]

$$\|\vec{u} - \vec{u}_h\|_s^2 = \int_{\Omega} \Delta \vec{\varepsilon}^T \Delta \vec{\tau} d\Omega \quad \text{with} \quad \Delta \vec{\varepsilon} = \vec{\varepsilon} - \vec{\varepsilon}_h, \quad \Delta \vec{\tau} = \vec{\tau} - \vec{\tau}_h, \quad (3.46)$$

where  $\vec{u}$  is the exact solution,  $\vec{u}_h$  is the solution of the finite element discretization, and  $\vec{\varepsilon}$  and  $\vec{\tau}$  are the strain and stress vectors. The s-norm is suitable to identify whether the finite element formulation satisfies the consistency and inf-sup conditions [2,41-43].

Instead of the exact solution  $\vec{u}$ , an accurate finite element solution using a very fine mesh  $\vec{u}_{ref}$  can be employed. Then the s-norm in Eq. (3.46) becomes

$$\|\vec{u}_{ref} - \vec{u}_h\|_s^2 = \int_{\Omega_{ref}} \Delta \vec{\varepsilon}^T \Delta \vec{\tau} d\Omega_{ref} \quad \text{with} \quad \Delta \vec{\varepsilon} = \vec{\varepsilon}_{ref} - \vec{\varepsilon}_h, \quad \Delta \vec{\tau} = \vec{\tau}_{ref} - \vec{\tau}_h. \quad (3.47)$$

To measure the performance of finite elements in shell analyses, it is important to consider decreasing shell thickness values. We then use the relative error  $E_h$

$$E_h = \frac{\|\vec{u}_{ref} - \vec{u}_h\|_s^2}{\|\vec{u}_{ref}\|_s^2}. \quad (3.48)$$

The optimal convergence behavior of the elements, for the shell problems considered, is given by

$$E_h \cong Ch^k, \quad (3.49)$$

in which  $h$  is the element size. For a 3-node shell element to be uniformly optimal, the value of  $C$  must be constant, that is, independent of the shell thickness, and  $k = 2$ .

In this study, well-converged reference solutions calculated using fine meshes of the MITC9 shell elements are used. The MITC9 shell element satisfies the ellipticity and consistency conditions and shows a good convergence behavior [22,41–45].

### 3.6.1 Fully clamped square plate problem

The plate bending problem shown in Fig. 3.12 is considered. A square plate of dimensions  $2L \times 2L$  with uniform thickness  $t$  is subjected to uniform pressure normal to the flat surface and all the edges are fully clamped. Due to symmetry, only a one-quarter model is considered, with the following boundary conditions imposed:  $u_x = \theta_y = 0$  along BC,  $u_y = \theta_x = 0$  along DC and  $u_x = u_y = u_z = \theta_x = \theta_y = 0$  along AB and AD [10,11].

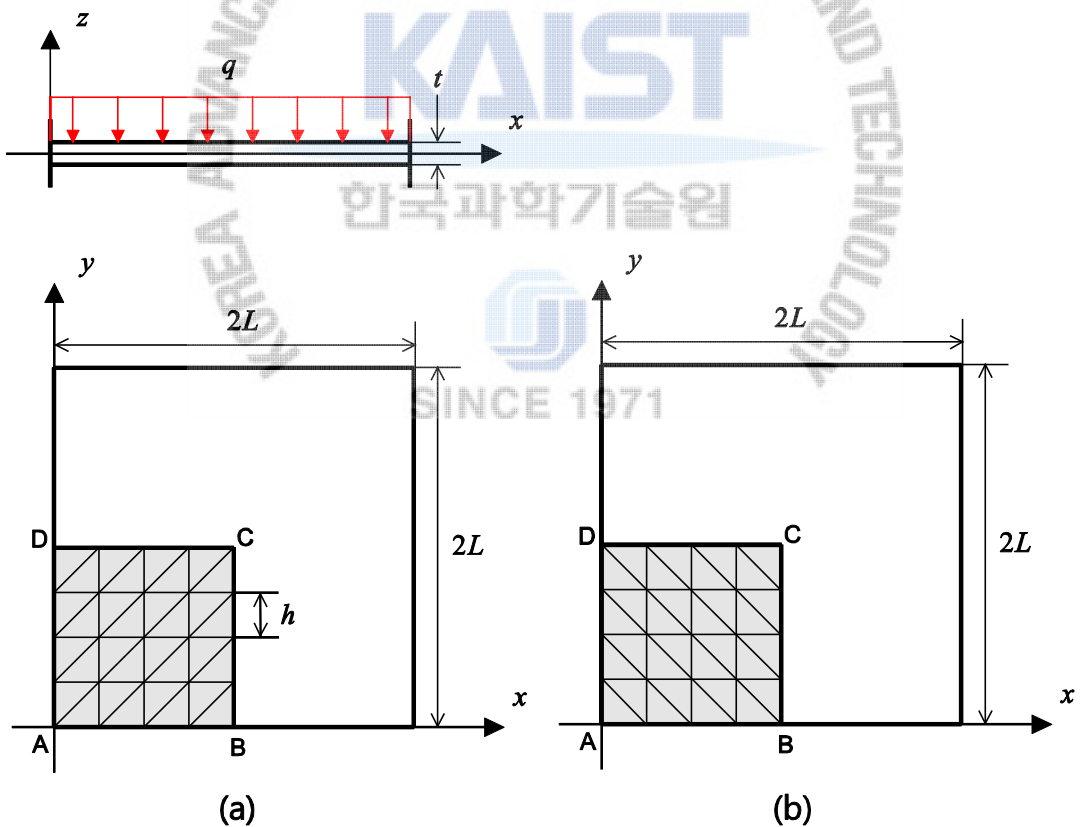


Fig. 3.12 Fully clamped square plate problem under uniform pressure ( $L=1.0$ ,  $E=1.7472 \times 10^7$ ,  $q=1.0$  and  $\nu=0.3$ ) with 2 different  $4 \times 4$  mesh patterns in (a) and (b).

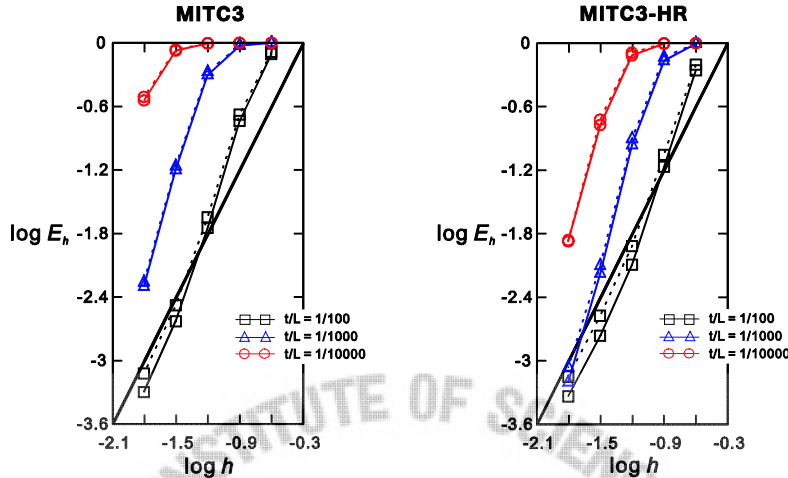


Fig. 3.13 Convergence curves for the fully clamped square plate problem. The bold line represents the optimal convergence rate. The solid and dotted lines correspond to the results obtained by the mesh patterns in Figs. 3.12(a) and (b), respectively.

The convergence curves of the MITC3 and MITC3-HR shell elements calculated by Eq. (3.48) are shown in Fig. 3.13. The reference solution is obtained by a mesh of  $96 \times 96$  MITC9 shell finite elements. The solutions of the MITC3 and MITC3-HR shell finite elements are calculated by  $N \times N$  meshes ( $N = 4, 8, 16, 32$  and  $64$ ). The element size is  $h = L/N$ . For the range of  $t/L(1/100, 1/1000, \text{ and } 1/10000)$  considered, the performance of the MITC3-HR shell finite element is much better than that of the MITC3 shell finite element.

The convergence studies with the distorted meshes shown in Fig. 3.14 are performed. When an  $N \times N$  element mesh is used, each edge is discretized in the following ratio:  $L_1 : L_2 : L_3 : \dots : L_N = 1 : 2 : 3 : \dots : N$ . Fig. 3.15 present the convergence curves for the tested elements, respectively. The MITC3-HR shell element shows improved performance than the MITC3 shell element.

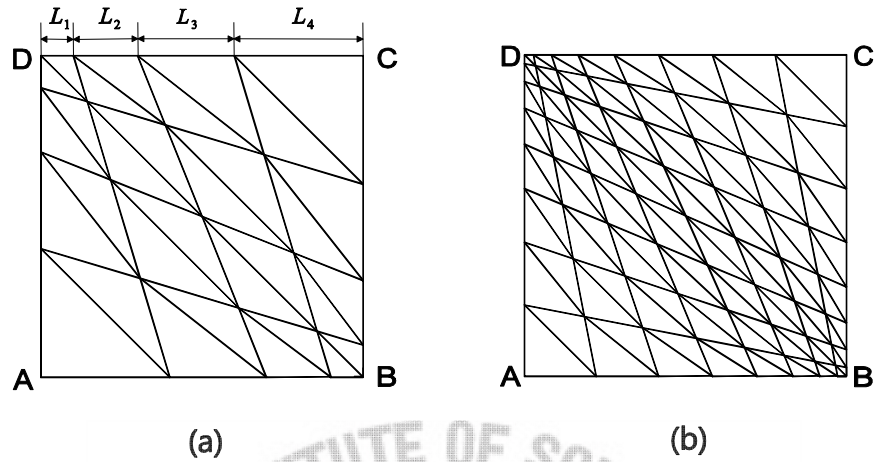


Fig. 3.14 Distorted mesh patterns (a) for  $N = 4$  and (b) for  $N = 8$ .

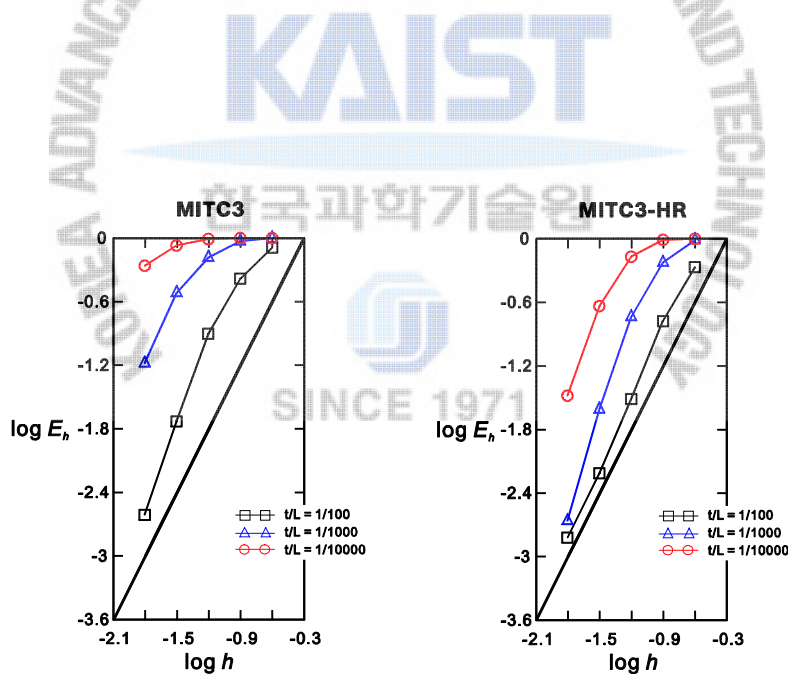


Fig. 3.15 Convergence curves for the fully clamped square plate problem with the distorted meshes shown in Fig. 3.14. The bold line represents the optimal convergence rate.

### 3.6.2 Simply supported sixty-degreeskew plate problem

Here the sixty-degree skew plate bending problem shown in Fig. 3.16 is solved. The simply supported skew plate with its edges of length  $2L$  and uniform thickness  $t$  is subjected to a uniform pressure. The boundary condition  $u_z = 0$  is imposed along all edges [40].

Fig. 3.17 shows the convergence curves of the MITC3 and MITC3-HR shell finite elements in the simply supported skew plate problem. A mesh of  $128 \times 128$  MITC9 shell finite elements is used for the calculation of the reference solution.  $N \times N$  meshes ( $N = 8, 16, 32, 64$ , and  $128$ ) are used to evaluate the solutions of the MITC3 and MITC3-HR shell finite elements. The element size is  $h = 2L/N$ . The graphs indicate the improved capability of the MITC3-HR shell finite element compared with the original MITC3 element.

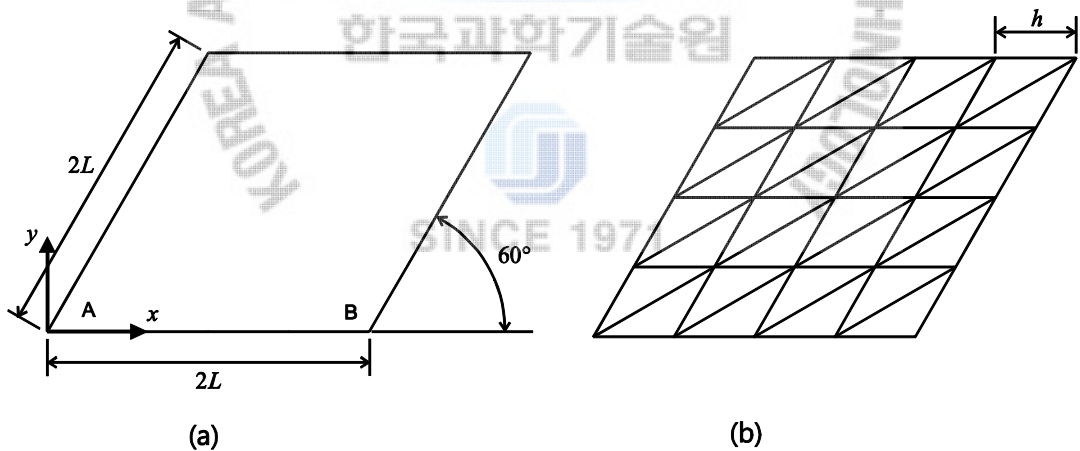


Fig. 3.16 Simply supported sixty-degree skew plate problem ( $L=1.0$ ,  $E=1.7472 \times 10^7$  and  $\nu=0.3$ ). (a) Problem description. (b) Mesh pattern used for  $N=4$ .

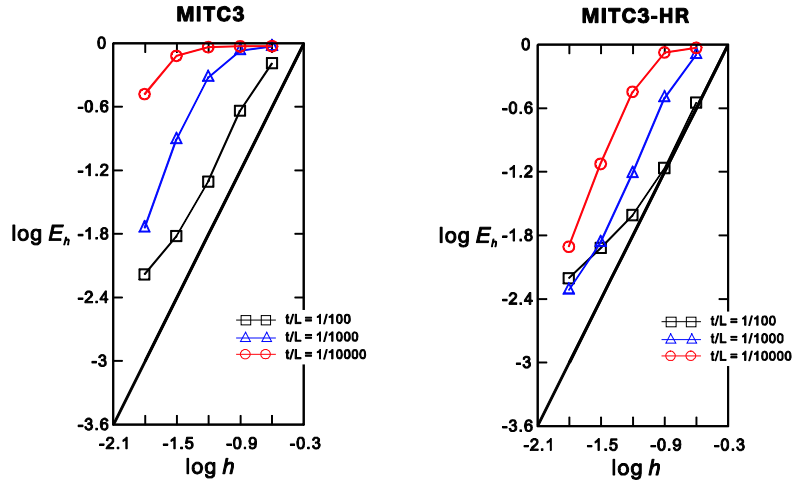


Fig. 3.17 Convergence curves for the simply supported sixty-degree skew plate problem. The bold line represents the optimal convergence rate.

### 3.6.3 Cylindrical shell problems

The cylindrical shell of length  $2L$ , radius  $R$  and uniform thickness  $t$  is considered as shown in Fig. 3.18.

The loading is a smoothly varying pressure  $p(\theta)$

$$p(\theta) = p_0 \cos(2\theta). \quad (3.50)$$

This shell structure shows different asymptotic behaviors depending on the boundary conditions at its ends. When both ends are free, a bending dominated problem is solved, whereas when both ends are clamped, a membrane dominated problem is considered.

Using symmetry, only the region ABCD in Fig. 3.18 is modeled. To have the membrane dominated problem, the clamped boundary condition is imposed:  $u_x = \beta = 0$  along BC,  $u_y = \alpha = 0$  along DC,  $u_z = \alpha = 0$  along AB, and  $u_x = u_y = u_z = \alpha = \beta = 0$  along AD. To have the bending dominated problem, the free boundary condition is imposed:  $u_x = \beta = 0$  along BC,  $u_y = \alpha = 0$  along DC, and  $u_z = \alpha = 0$  along AB.

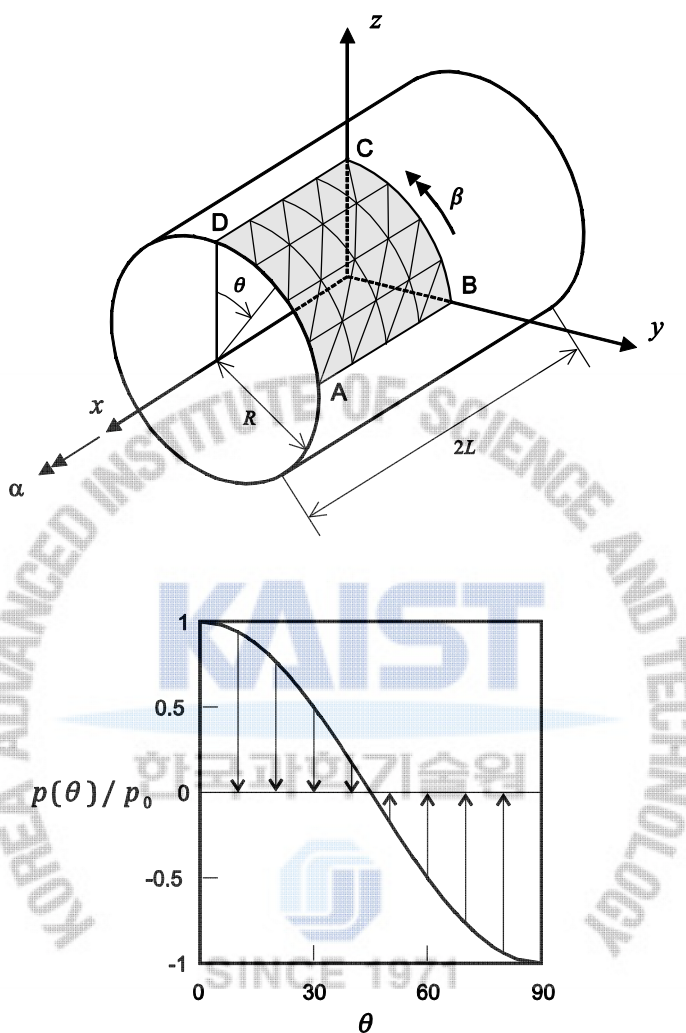


Fig. 3.18 Cylindrical shell problem ( $4 \times 4$  mesh,  $L = R = 1.0$ ,  $E = 2.0 \times 10^5$ ,  $\nu = 1/3$  and  $p_0 = 1.0$ ).

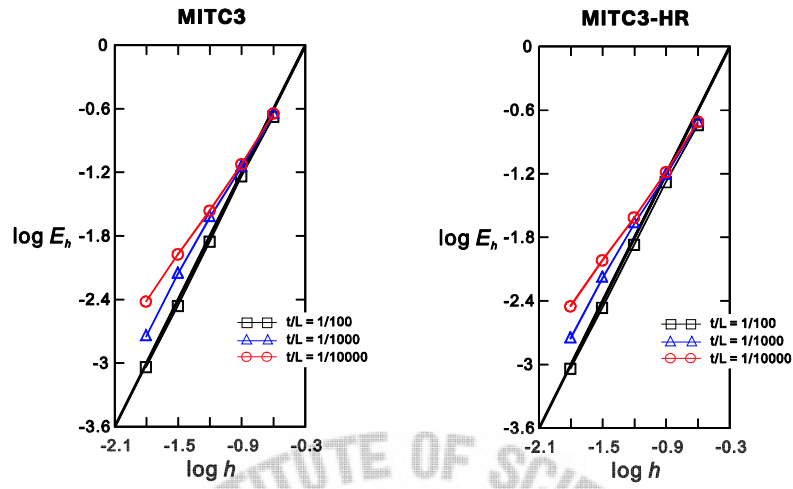


Fig. 3.19 Convergence curves for the clamped cylindrical shell problem. The bold line represents the optimal convergence rate.

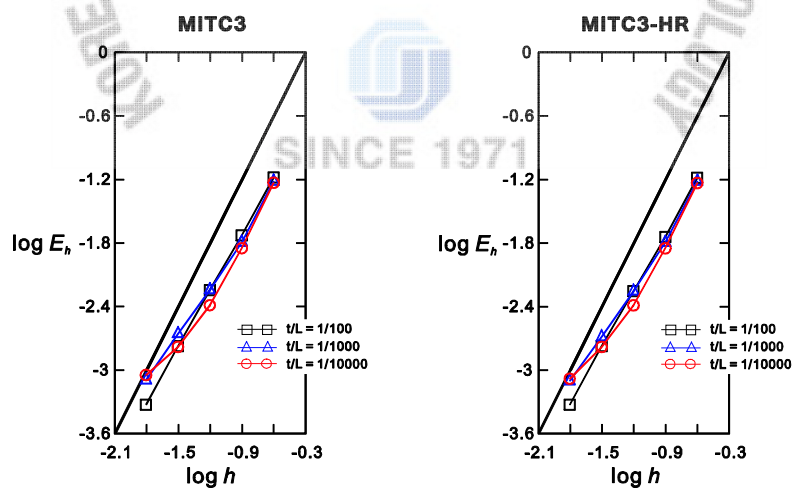


Fig. 3.20 Convergence curves for the free cylindrical shell problem. The bold line represents the optimal convergence rate.

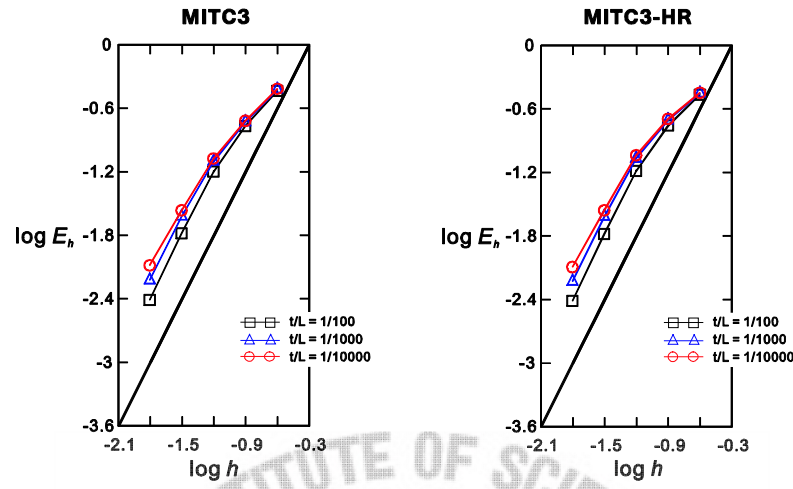


Fig. 3.21 Convergence curves for the clamped cylindrical shell problem with the distorted meshes shown in Fig. 3.14. The bold line represents the optimal convergence rate.

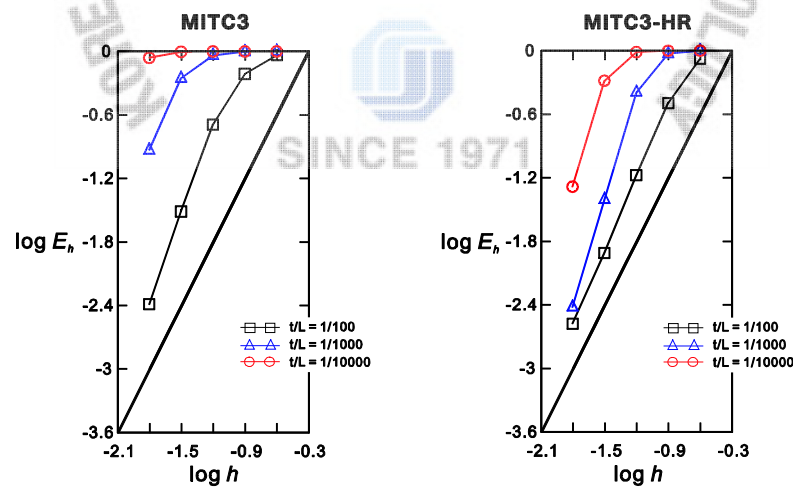


Fig. 3.22 Convergence curves for the free cylindrical shell problem with the distorted meshes shown in Fig. 3.14. The bold line represents the optimal convergence rate.

Figs. 3.19 and 3.20 present the convergence behaviors of the MITC3 and MITC3-HR shell finite elements for the clamped and free cylindrical shell problems, respectively. The reference solution is calculated by a mesh of  $96 \times 96$  MITC9 shell finite elements for both cases. The solutions of the MITC3 and MITC3-HR shell finite elements are obtained by  $N \times N$  meshes ( $N = 4, 8, 16, 32$ , and  $64$ ). The element size is  $h = L/N$ . Excellent convergence behavior of the MITC3 element in the cylindrical shell problems has been reported in Ref. [10]. The MITC3-HR shell finite element similarly shows excellent convergence behavior.

Figs. 3.21 and 3.22 give the convergence curves of the MITC3 and MITC3-HRshell elements when the distorted meshes in Fig. 3.14 are used. In the membrane dominated problem, the testes shell elements show similarly good convergence behavior. In the bending dominated problem, the MITC3-HR presents improved capability compared with the original MITC3 element.

### 3.6.4 Hyperboloid shell problems

Finally, the hyperboloid shell shown in Fig. 3.23 is considered. The mid-surface of the shell structure is given by

$$x^2 + z^2 = 1 + y^2; y \in [-1, 1]. \quad (3.51)$$

As for the cylindrical shell problems, a smoothly varying pressure is applied, see Fig. 3.18,

$$p(\theta) = p_0 \cos(2\theta). \quad (3.52)$$

A bending dominated behavior is obtained with free ends and a membrane dominated behavior is given with clamped ends. The bending dominated problem is known to be difficult to solve accurately [2].

Due to symmetry, the analyses are performed using one-eighth of the structure corresponding to the shaded region ABCD in Fig. 3.23(a). For the membrane dominated case, the clamped boundary condition is imposed:  $u_z = \beta = 0$  along BC,  $u_x = \beta = 0$  along AD, and  $u_y = \alpha = 0$  along DC, and  $u_x = u_y = u_z = \alpha = \beta = 0$  along AB. For the bending dominated case, the free boundary condition is imposed:  $u_z = \beta = 0$  along BC,  $u_x = \beta = 0$  along AD, and  $u_y = \alpha = 0$  along DC.

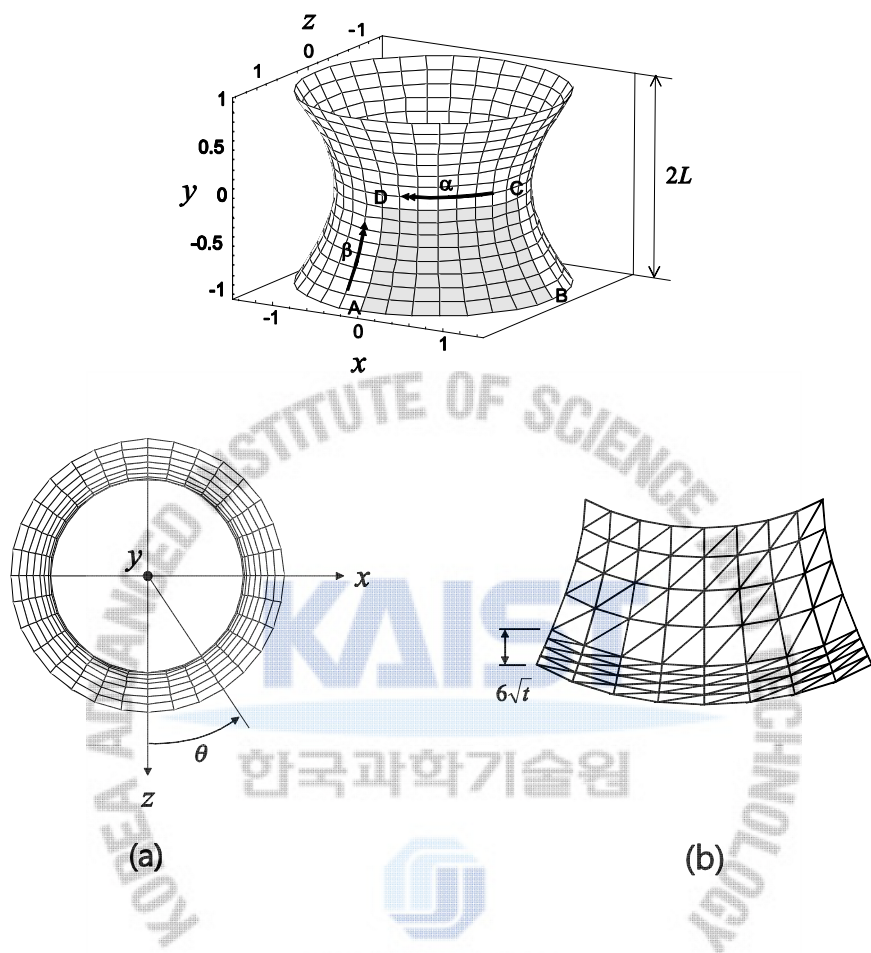


Fig. 3.23 Hyperboloid shell problem ( $E=2.0\times10^{11}$ ,  $\nu=1/3$  and  $p_0=1.0$ ). (a) Problem description. (b) Graded mesh for the clamped case (8×8 mesh,  $t/L=1/1000$ ).

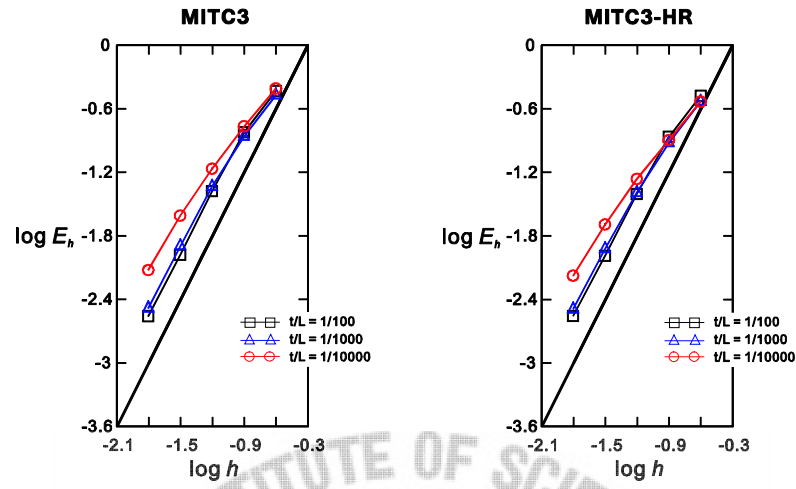


Fig. 3.24 Convergence curves for the clamped hyperboloid shell problem. The bold line represents the optimal convergence rate.

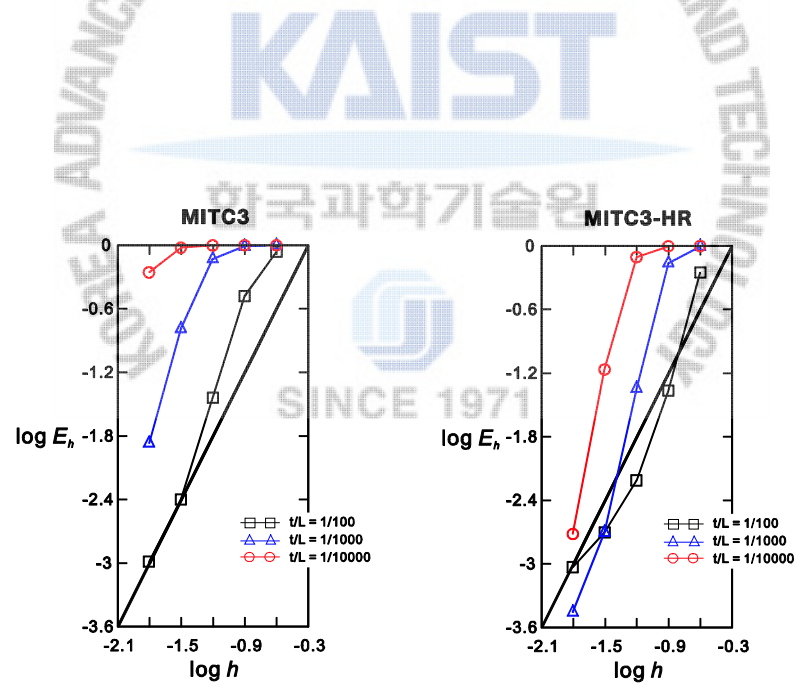


Fig. 3.25 Convergence curves for the free hyperboloid shell problem. The bold line represents the optimal convergence rate.

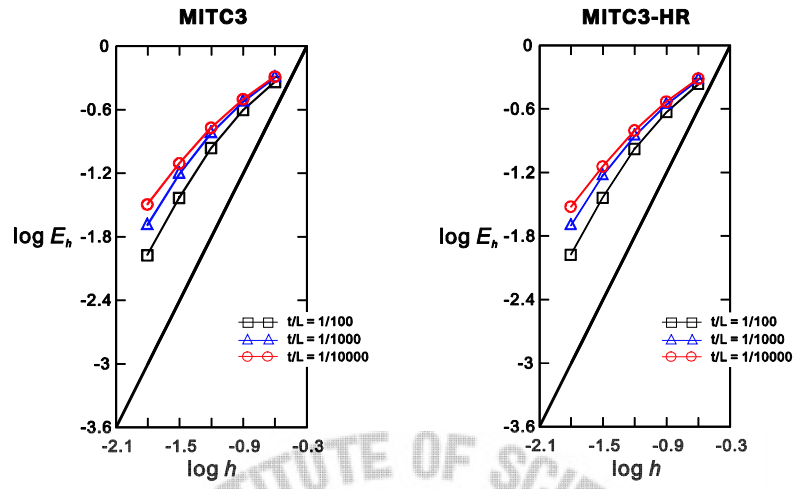


Fig. 3.26 Convergence curves for the clamped hyperboloid shell problem with the distorted meshes shown in Fig. 3.14. The bold line represents the optimal convergence rate.

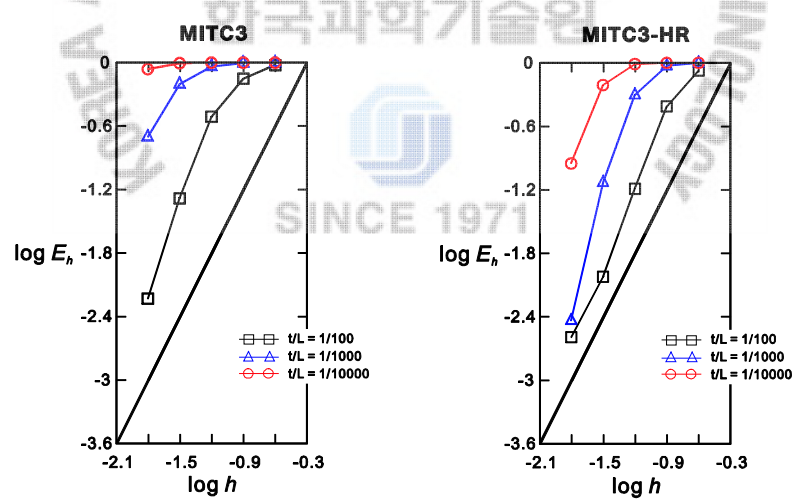


Fig. 3.27 Convergence curves for the free hyperboloid shell problem with the distorted meshes shown in Fig. 3.14. The bold line represents the optimal convergence rate.

In both cases, a  $96 \times 96$  element mesh of MITC9 shell elements is used to obtain the reference solutions. The solutions of the MITC3, MITC3i and MITC3+ shell elements are calculated using  $N \times N$  element meshes ( $N = 4, 8, 16, 32$  and  $64$ ). The element size is  $h = L/N$ . In the clamped hyperboloid shell case, a boundary layer of width  $6\sqrt{t}$  is considered for half of the mesh, see Fig. 3.23(b). In the free hyperboloid shell case, the thin boundary layer is not specially considered [2].

For both the membrane and bending dominated cases, the convergence curves are shown in Figs. 3.24 and 3.25. In the membrane dominated case (that is, the clamped hyperboloid shell problem), the performance of the MITC3-HR shell finite element is almost the same as that of the MITC3 shell finite element. Fig. 3.25 displays the substantially improved performance of the MITC3-HR shell finite element compared to the MITC3 shell finite element.

Figs. 3.26 and 3.27 give the convergence curves of the MITC3 and MITC3-HR shell elements when the distorted meshes in Fig. 3.14 are used. In the membrane dominated case, the MITC3 and MITC3-HR shell finite element shows similar convergence behavior. However, in the bending dominated cases, the MITC3-HR shell element presents better performance than the MITC3 shell element.

### 3.7 Closure

The MITC3-HR shell finite element was developed by using the modified Hellinger-Reissner (HR) functional and applying the proposed rotated approximated transverse shear strain field. The results of the basic numerical tests show that the MITC3-HR shell finite element satisfies all the basic requirements. The results of the convergence studies proved that the MITC3 shell finite element is successfully improved; that is, the MITC3-HR shell finite element shows much better convergence behavior than the MITC3 shell finite element, especially in bending-dominated problems. From these studies and Appendix A, it is investigated that the stiffness of the in-plane twisting mode should be reduced to improve 3-node triangular shell elements. Also, bending displacements should be enriched to obtain better results than the MITC3-HR shell element in convergence tests because a 3-node triangular shell element lacks bending displacements.

## Chapter 4.MITC3+ shell finite element

In general, 3-node triangular elements for the two-dimensional analysis of solids and the analysis of shells suffer from a lack of displacement modes [1,11,12]. To overcome this inherent limitation in some elements, a scheme to enrich the displacement field can be effective [46-50]. In particular, bubble functions have been used to improve the predictive capability of finite elements for two- and three-dimensional solid and fluid flow analyses, and for plate and shell solutions [1,22, 47, 50-53]. A cubic bubble function for a 3-node triangular element is attractive [47, 50] because it provides a higher-order interpolation inside the element while maintaining the linear interpolation along the element edges, thus providing compatibility between elements.

In the development of the new triangular 3-node shell element, which we call the MITC3+ shell element, we use a cubic bubble function for the interpolation of the rotations to enrich the bending displacements. That is, only 2 internal rotation degrees of freedom are added to the standard 3-node shell element. Hence, the bubble function does not affect the mid-surface displacement of the shell element, and the corresponding degrees of freedom can be statically condensed out on the element level [24].

### 4.1 Geometry and displacement interpolation



The geometry interpolation of the MITC3+ shell element, shown in Fig. 4.1, is given by

$$\vec{x}(r,s,t) = \sum_{i=1}^3 h_i(r,s) \vec{x}_i + \frac{t}{2} \sum_{i=1}^4 a_i f_i(r,s) \vec{V}_n^i \quad \text{with} \quad a_4 \vec{V}_n^4 = \frac{1}{3} (a_1 \vec{V}_n^1 + a_2 \vec{V}_n^2 + a_3 \vec{V}_n^3), \quad (4.1)$$

in which the  $f_i(r,s)$  are two-dimensional interpolation functions that include the cubic bubble function  $f_4$  corresponding to the internal node 4

$$f_1 = h_1 - \frac{1}{3} f_4, \quad f_2 = h_2 - \frac{1}{3} f_4, \quad f_3 = h_3 - \frac{1}{3} f_4, \quad f_4 = 27rs(1-r-s). \quad (4.2)$$

From Eq. (3.1), we obtain the displacement interpolation [10]

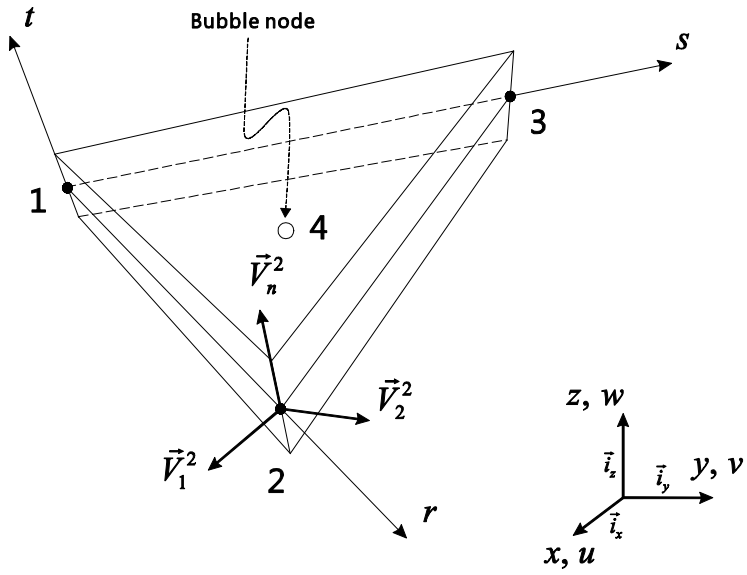


Fig. 4.1 Geometry of the MITC3+ shell element with an additional bubble node.

$$\vec{u}(r, s, t) = \sum_{i=1}^3 h_i(r, s) \vec{u}_i + \frac{t}{2} \sum_{i=1}^4 a_i f_i(r, s) (-\vec{V}_2^i \alpha_i + \vec{V}_1^i \beta_i), \quad (4.3)$$

in which  $\alpha_4$  and  $\beta_4$  are the rotation degrees of freedom at the bubble node.

The bubble node, with rotation degrees of freedom only, is positioned on the flat surface defined by the three corner nodes of the element. Only the bending and shear fields are enriched by the bubble function, and the geometry of the element would remain flat, as for the MITC3 element, if a large deformation analysis were pursued. Hence, the membrane locking is no present and it is so effective in geometric nonlinear analysis. Also, static condensation can be carried out on the element level for the rotations  $\alpha_4$  and  $\beta_4$ .

#### 4.2 Assumed transverse shear strain field

As for the MITC3 shell element, we only use the mixed interpolation for the transverse shear strain components, but we must design a new assumed transverse shear strain field because the effect of the bubble function should be included.

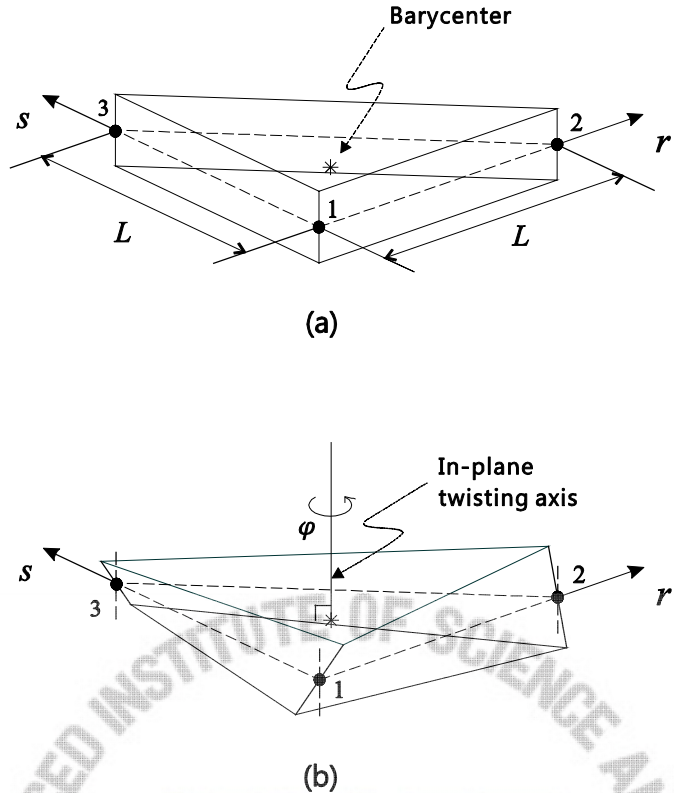


Fig. 4.2 In-plane twisting mode of a single shell finite element. (a) Undeformed geometry. (b) In-plane twisting mode.

To design the new assumed transverse shear strain field, we focus on two considerations. Firstly, the tying points for the covariant transverse shear strain components should be inside the element, that is, not on the element edges as for the MITC3 element, because the bubble function is zero along the element edges. Secondly, the stiffness of the in-plane twisting mode, see Fig. 4.2 must be reduced [12].

Considering a 3-node triangular shell element (that is, without the node for the bubble), the transverse shear strains occur in two transverse shearing modes and in an in-plane twisting mode. The in-plane twisting mode corresponds to twisting of the element about the axis normal to the mid-surface at the barycenter,  $r = s = 1/3$ , as shown in Fig. 4.2, with zero transverse shear strains at that point.

The transverse shear strain field of the MITC3 shell element in Eq. (3.13) can be separated into the constant part corresponding to the transverse shearing modes and the linear part corresponding to the in-plane twisting mode

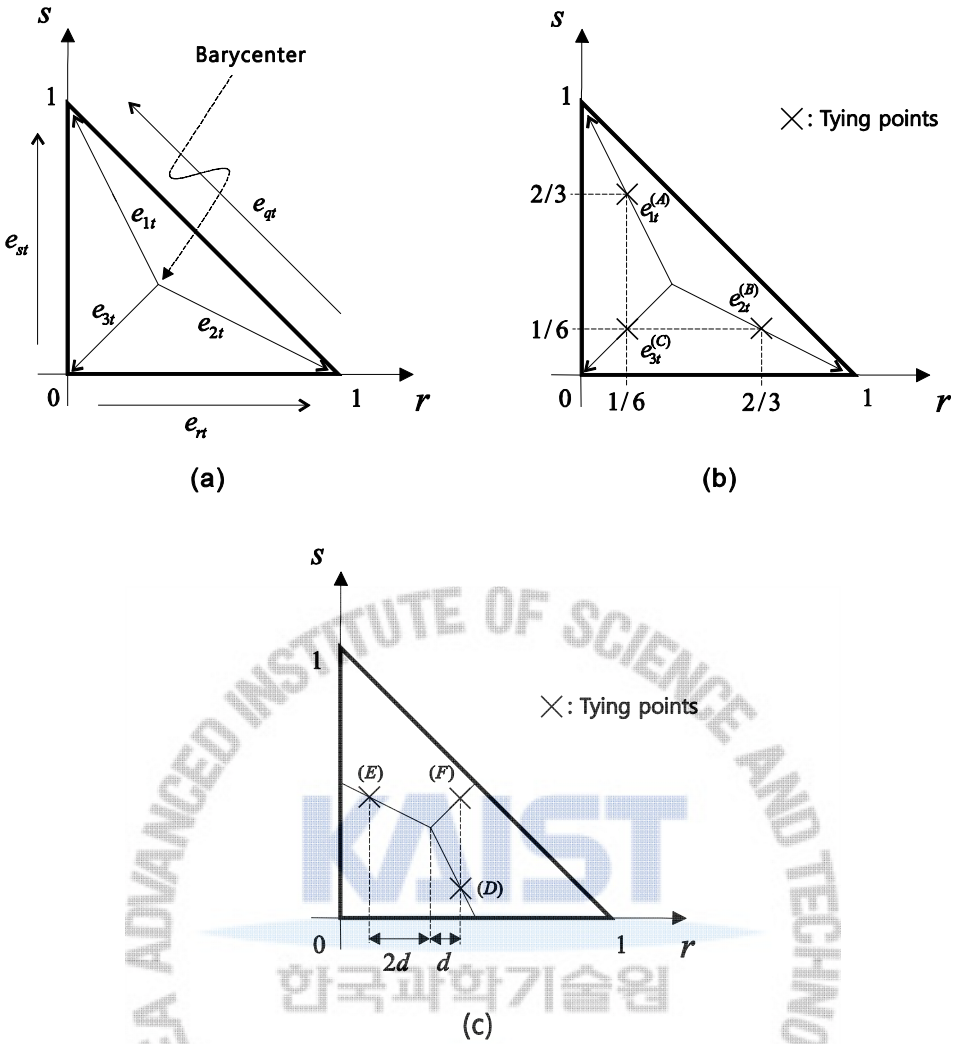


Fig. 4.3 Transverse shear strains  $e_{1t}$ ,  $e_{2t}$  and  $e_{3t}$ , and the tying positions (A)-(F) for the new assumed transverse shear strain field.

$$\tilde{e}_{rt}^{MITC3} = \tilde{e}_{rt}^{const.} + \tilde{e}_{rt}^{linear}, \quad \tilde{e}_{st}^{MITC3} = \tilde{e}_{st}^{const.} + \tilde{e}_{st}^{linear}. \quad (4.4)$$

We can easily obtain the constant part by evaluating the transverse shear strains at the barycenter

$$\begin{aligned} \tilde{e}_{rt}^{const.} &= \tilde{e}_{rt}^{MITC3} \Big|_{s=1/3} = \frac{2}{3}(e_{rt}^{(1)} + \frac{1}{2}e_{st}^{(2)}) - \frac{1}{3}(e_{st}^{(3)} - e_{rt}^{(3)}), \\ \tilde{e}_{st}^{const.} &= \tilde{e}_{st}^{MITC3} \Big|_{r=1/3} = \frac{2}{3}(e_{st}^{(2)} + \frac{1}{2}e_{rt}^{(1)}) + \frac{1}{3}(e_{st}^{(3)} - e_{rt}^{(3)}). \end{aligned} \quad (4.5)$$

Subtracting, for the MITC3 shell element, the constant part from the transverse shear strain field in Eq. (3.13), we obtain the linearly varying part

$$\begin{aligned}\tilde{e}_{rt}^{linear} &= \tilde{e}_{rt}^{MITC3} - \tilde{e}_{rt}^{const.} = \frac{1}{3}c(3s-1), \\ \tilde{e}_{st}^{linear} &= \tilde{e}_{st}^{MITC3} - \tilde{e}_{st}^{const.} = \frac{1}{3}c(1-3r).\end{aligned}\quad (4.6)$$

If this scheme were used for the new element, the constant part in Eq. (4.5) would not include the effect of the bubble function since the bubble function is zero along the element edges, that is, at the tying positions (1), (2) and (3). To include the effect of the bubble function in the constant part, we design a new tying scheme using element internal points. First, the three covariant transverse shear strains  $e_{1t}$ ,  $e_{2t}$  and  $e_{3t}$  are defined in the directions of the internal lines from the barycenter to the corners as shown in Fig. 4.3(a). The following vector relations are obtained for the covariant transverse shear strain components, for  $0 \leq r, s \leq 1$ ,

$$e_{1t} = \frac{1}{\sqrt{5}}(2e_{st} - e_{rt}), \quad e_{2t} = \frac{1}{\sqrt{5}}(2e_{rt} - e_{st}), \quad e_{3t} = -\frac{1}{\sqrt{2}}(e_{rt} + e_{st}), \quad (4.7a)$$

and

$$e_{rt} = \frac{\sqrt{5}}{3}e_{2t} - \frac{\sqrt{2}}{3}e_{3t}, \quad e_{st} = \frac{\sqrt{5}}{3}e_{1t} - \frac{\sqrt{2}}{3}e_{3t}, \quad e_{qt} = \frac{1}{\sqrt{2}}(e_{st} - e_{rt}) = \frac{\sqrt{10}}{6}(e_{1t} - e_{2t}). \quad (4.7b)$$

Using Eq. (4.7a), the transverse shear strain components are sampled at three internal tying points (A), (B) and (C) on the three internal lines, see Fig. 4.3(b) Table 4.1

$$e_{1t}^{(A)} = \frac{1}{\sqrt{5}}(2e_{st}^{(A)} - e_{rt}^{(A)}), \quad e_{2t}^{(B)} = \frac{1}{\sqrt{5}}(2e_{rt}^{(B)} - e_{st}^{(B)}), \quad e_{3t}^{(C)} = -\frac{1}{\sqrt{2}}(e_{st}^{(C)} + e_{rt}^{(C)}). \quad (4.8)$$

It is important to note that the tying points have been selected to obtain a spatially isotropic element.

Using next the relations in Eq. (4.7b), the constant covariant transverse shear strains along the element edge directions are assumed to be

$$\hat{e}_{rt} = \frac{\sqrt{5}}{3}e_{2t}^{(B)} - \frac{\sqrt{2}}{3}e_{3t}^{(C)}, \quad \hat{e}_{st} = \frac{\sqrt{5}}{3}e_{1t}^{(A)} - \frac{\sqrt{2}}{3}e_{3t}^{(C)}, \quad \hat{e}_{qt} = \frac{\sqrt{10}}{6}(e_{1t}^{(A)} - e_{2t}^{(B)}), \quad (4.9)$$

and, using Eq. (4.8), a new constant transverse shear strain field is obtained

$$\begin{aligned}\hat{e}_{rt}^{const.} &= \hat{e}_{rt} = \frac{2}{3}(e_{rt}^{(B)} - \frac{1}{2}e_{st}^{(B)}) + \frac{1}{3}(e_{rt}^{(C)} + e_{st}^{(C)}), \\ \hat{e}_{st}^{const.} &= \hat{e}_{st} = \frac{2}{3}(e_{st}^{(A)} - \frac{1}{2}e_{rt}^{(A)}) + \frac{1}{3}(e_{rt}^{(C)} + e_{st}^{(C)}).\end{aligned}\quad (4.10)$$

In order to render the in-plane twisting stiffness more flexible, the linear part is modified by using three new tying points (D), (E) and (F) instead of the tying points (1), (2) and (3) when we evaluate  $c$  in Eq. (4.6)

$$\hat{e}_{rt}^{linear} = \frac{1}{3}\hat{c}(3s-1), \quad \hat{e}_{st}^{linear} = \frac{1}{3}\hat{c}(1-3r) \quad \text{with } \hat{c} = (e_{rt}^{(F)} - e_{rt}^{(D)}) - (e_{st}^{(F)} - e_{st}^{(E)}). \quad (4.11)$$

The tying positions (D), (E) and (F) are positioned on the three internal lines from the barycenter to the centers of the edges with  $d$  defined in Fig. 4.3(c) and Table 4.1. As  $d$  varies from  $1/6$  to 0, the three tying positions move from the centers of the edges to the barycenter, resulting in a smaller in-plane twisting stiffness. An effective value for  $d$  is determined below.

The new assumed transverse shear strain field is thus given by

$$\begin{aligned} \hat{e}_{rt} &= \hat{e}_{rt}^{const.} + \hat{e}_{rt}^{linear} = \frac{2}{3}(e_{rt}^{(B)} - \frac{1}{2}e_{st}^{(B)}) + \frac{1}{3}(e_{rt}^{(C)} + e_{st}^{(C)}) + \frac{1}{3}\hat{c}(3s-1), \\ \hat{e}_{st} &= \hat{e}_{st}^{const.} + \hat{e}_{st}^{linear} = \frac{2}{3}(e_{st}^{(A)} - \frac{1}{2}e_{rt}^{(A)}) + \frac{1}{3}(e_{rt}^{(C)} + e_{st}^{(C)}) + \frac{1}{3}\hat{c}(1-3r). \end{aligned} \quad (4.12)$$

At this point, it is interesting to consider a 3-node shell finite element in which the geometry and displacement interpolations in Eqs. (3.1) and (3.2) and the new assumed transverse shear strain field in Eq. (4.12) are employed. We label this element as MITC3i and study its performance as well in the following sections. Also, other new assumed transverse shear strain fields are presented using the new tying scheme in Appendix B.



Table 4.1 Tying positions for the new assumed transverse shear strain field for the MITC3i and MITC3+ shell elements. The distance  $d$  is defined in Fig. 4.3(c).

	Tying positions	$r$	$s$
Fig. 4.3(b)	(A)	$1/6$	$2/3$
	(B)	$2/3$	$1/6$
	(C)	$1/6$	$1/6$
Fig. 4.3(c)	(D)	$1/3+d$	$1/3-2d$
	(E)	$1/3-2d$	$1/3+d$
	(F)	$1/3+d$	$1/3+d$

### 4.3. Basic numerical tests

In this section, we consider the three basic tests: the isotropy, patch and zero energy mode tests. Table 4.2 presents the results of the basic tests.

The spatially isotropic behavior is an important requirement for triangular shell elements. The element behavior should not depend on the sequence of node numbering, i.e. the element orientation [1]. The numerical procedure for the isotropy element test is given in Section 3.5.2. The MITC3i and MITC3+shell elements pass this test.

Three patch tests are performed: the membrane, bending and shearing patch tests, see Ref [1] for the patch tests performed, see Section 3.5.3. The constant stress fields should be calculated to pass the patch tests. The MITC3i and MITC3+ shell elements pass the three patch tests.

In the zero energy mode test, the number of zero eigenvalues of the stiffness matrix of a single unsupported element are counted [1,2]. For the MITC3i and MITC3+ shell elements, only the six zero eigenvalues corresponding to the six rigid body modes are obtained when the distance  $d$  defined for the tying positions (D), (E) and (F) in Fig. 4.3(c) is non-zero. As  $d$  approaches 0, the eigenvalue corresponding to the in-plane twisting mode in Fig. 4.2 decreases and is zero when  $d = 0$ .

A similar phenomenon was investigated for the MITC3-HR shell element in Ref. [12], where it was shown that by decreasing the stiffness for the in-plane twisting mode, it is possible to improve the performance of 3-node shell elements. Therefore, we perform the in-plane twisting mode test given in Ref. [12] and investigate the effect of the distance  $d$ .

Table 4.2 Results of basic numerical tests.

Element	Zero energy mode test	Isotropy test	Patch test
MITC3+	Pass	Pass	Pass
MITC3i	Pass	Pass	Pass

The strain energies ( $E_t$ ) of the MITC3i and MITC3+shell elements are calculated when the elements are subjected to the in-plane twisting mode in Fig. 4.2. We use  $L=1.0$ ,  $E=1.7472 \times 10^7$  and  $\nu=0.3$ . The in-plane twisting mode is given by prescribing the rotations at the nodes to be  $\theta_x^1 = \theta_x^3 = \theta_y^1 = \theta_y^2 = 1/\sqrt{12}$  and  $\theta_x^2 = \theta_y^3 = -2/\sqrt{12}$ . Fig. 4.4 gives the strain energies of the MITC3i and MITC3+shell elements as a function of the distance  $d$ . When the distance  $d$  approaches zero, both shell elements become rapidly more flexible in the in-plane twisting mode.

Tables 4.3 and 4.4 present the eigenvalues of the stiffness matrices of the MITC3i and MITC3+ shell elements for the element geometry shown in Fig. 4.2(a). We consider  $t/L=1/10,000$ ,  $E=1.7472 \times 10^7$  and  $\nu=0.3$ . The eigenvalue corresponding to the in-plane twisting mode decreases as the distance  $d$  decreases but is larger than the smallest eigenvalue of a bending mode. Based on this study we choose and always use the distance  $d=1/10,000$ . As a consequence, the element formulation contains no spurious zero energy mode, and the ellipticity condition is satisfied. Note that, due to the bubble function enrichment, the MITC3+ shell element contains two additional bending modes compared to the MITC3i shell element.

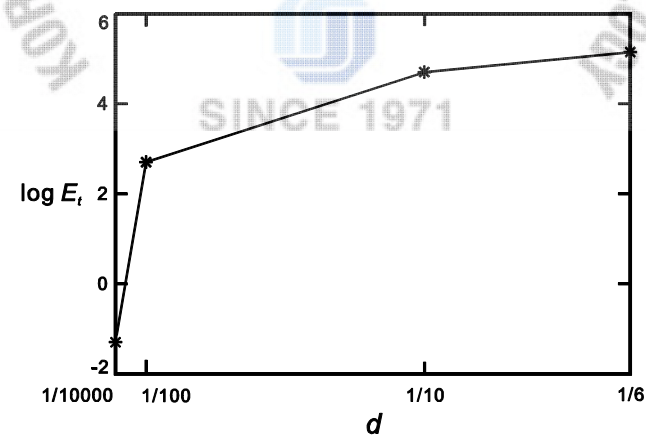


Fig. 4.4 Strain energy stored in the MITC3i and MITC3+ shell elements depending on the distance  $d$  in the in-plane twisting mode. Since the strain energy is proportional to  $t \cdot L^2$  in the in-plane twisting mode,  $E_t$  is the strain energy normalized by  $t \cdot L^2$ .

Table 4.3 Eigenvalues of the stiffness matrix of the single MITC3i shell element for the element geometry shown in Fig. 4.2(a) when  $t/L = 1/10,000$ . Note that modes 1 to 6 produce zero eigenvalues corresponding to rigid body modes.

Mode	$d = 1/6$		$d = 1/10$		$d = 1/100$		$d = 1/10,000$	
7	6.6764E-07	B	6.6764E-07	B	6.6764E-07	B	6.6764E-07	B
8	8.1455E-07	B	8.1455E-07	B	8.1454E-07	B	7.9792E-07	B
9	2.4924E-06	B	2.4924E-06	B	2.4924E-06	B	2.4924E-06	B
10	<u>3.6928E+01</u>	T	<u>1.3302E+01</u>	T	<u>1.3306E-01</u>	T	<u>1.3583E-05</u>	T
11	4.6707E+02	S	4.6681E+02	S	4.6667E+02	S	4.6667E+02	S
12	8.3813E+02	M	8.3813E+02	M	8.3813E+02	M	8.3813E+02	M
13	1.1760E+03	S	1.1760E+03	S	1.1760E+03	S	1.1760E+03	S
14	1.3440E+03	M	1.3440E+03	M	1.3440E+03	M	1.3440E+03	M
15	3.0019E+03	M	3.0019E+03	M	3.0019E+03	M	3.0019E+03	M

B: Bending modes, T: In-plane twisting mode, S: Transverse shearing modes, M: Membrane modes

Table 4.4 Eigenvalues of the stiffness matrix of the single MITC3+ shell element for the element geometry shown in Fig. 4.2(a) when  $t/L = 1/10,000$ . Note that modes 1 to 6 produce zero eigenvalues corresponding to rigid body modes.

Mode	$d = 1/6$		$d = 1/10$		$d = 1/100$		$d = 1/10,000$	
7	6.6685E-07	B	6.6685E-07	B	6.6685E-07	B	6.6685E-07	B
8	8.1273E-07	B	8.1273E-07	B	8.1272E-07	B	7.9621E-07	B
9	2.4921E-06	B	2.4921E-06	B	2.4921E-06	B	2.4921E-06	B
10	8.3211E-06	B+	8.3211E-06	B+	8.3211E-06	B+	8.3107E-06	B+
11	1.4128E-05	B+	1.4128E-05	B+	1.4128E-05	B+	<u>1.3599E-05</u>	T
12	<u>3.6928E+01</u>	T	<u>1.3302E+01</u>	T	<u>1.3306E-01</u>	T	1.4128E-05	B+
13	4.6707E+02	S	4.6681E+02	S	4.6667E+02	S	4.6667E+02	S
14	8.3813E+02	M	8.3813E+02	M	8.3813E+02	M	8.3813E+02	M
15	1.1760E+03	S	1.1760E+03	S	1.1760E+03	S	1.1760E+03	S
16	1.3440E+03	M	1.3440E+03	M	1.3440E+03	M	1.3440E+03	M
17	3.0019E+03	M	3.0019E+03	M	3.0019E+03	M	3.0019E+03	M

B: Bending modes, T: In-plane twisting mode, S: Transverse shearing modes, M: Membrane modes, B+: Bending modes due to the bubble function enrichment

#### 4.4 Convergence studies

In this section, the convergence studies are performed as constructed in Section 3.6. Also, the results of the tested elements are compared with those of the 4-node MITC4 quadrilateral shell element.

##### 4.4.1 Fully clamped square plate problem

The plate bending problem shown in Fig. 3.12 is solved. A square plate of dimensions  $2L \times 2L$  and uniform thickness  $t$  is subjected to a uniform pressure. All edges are fully clamped (in hard conditions [10]). Due to symmetry, only a one-quarter model is considered, with the following boundary conditions:  $u_x = \theta_y = 0$  along BC,  $u_y = \theta_x = 0$  along DC and  $u_x = u_y = u_z = \theta_x = \theta_y = 0$  along AB and AD.

Fig. 4.5 gives the convergence curves of the MITC3, MITC3i, MITC3+ and MITC4 elements. A  $96 \times 96$  element mesh of the MITC9 shell element is used to obtain the reference solution. We use  $N \times N$  element meshes ( $N = 4, 8, 16, 32$ , and  $64$ ) to calculate the solutions using the triangular shell elements. The element size in the convergence curves is  $h = L/N$ . The performance of the MITC3+ shell element is best among the triangular shell elements and, practically, uniformly optimal, like the MITC4 shell element.

The convergence studies with the distorted meshes shown in Fig. 3.14 are also performed. When an  $N \times N$  element mesh is used, each edge is discretized in the following ratio:  $L_1 : L_2 : L_3 : \dots : L_N = 1 : 2 : 3 : \dots : N$ . Fig. 4.6 presents the convergence curves for the tested elements, respectively. The MITC3+ shell element still shows an excellent performance.

##### 4.4.2 Simply supported sixty-degreeskew plate problem

Here the sixty-degree skew plate bending problem shown in Fig. 3.16 is considered. The simply supported skew plate with its edges of length  $2L$  and uniform thickness  $t$  is subjected to a uniform pressure. The boundary condition  $u_z = 0$  is imposed along all edges [40].

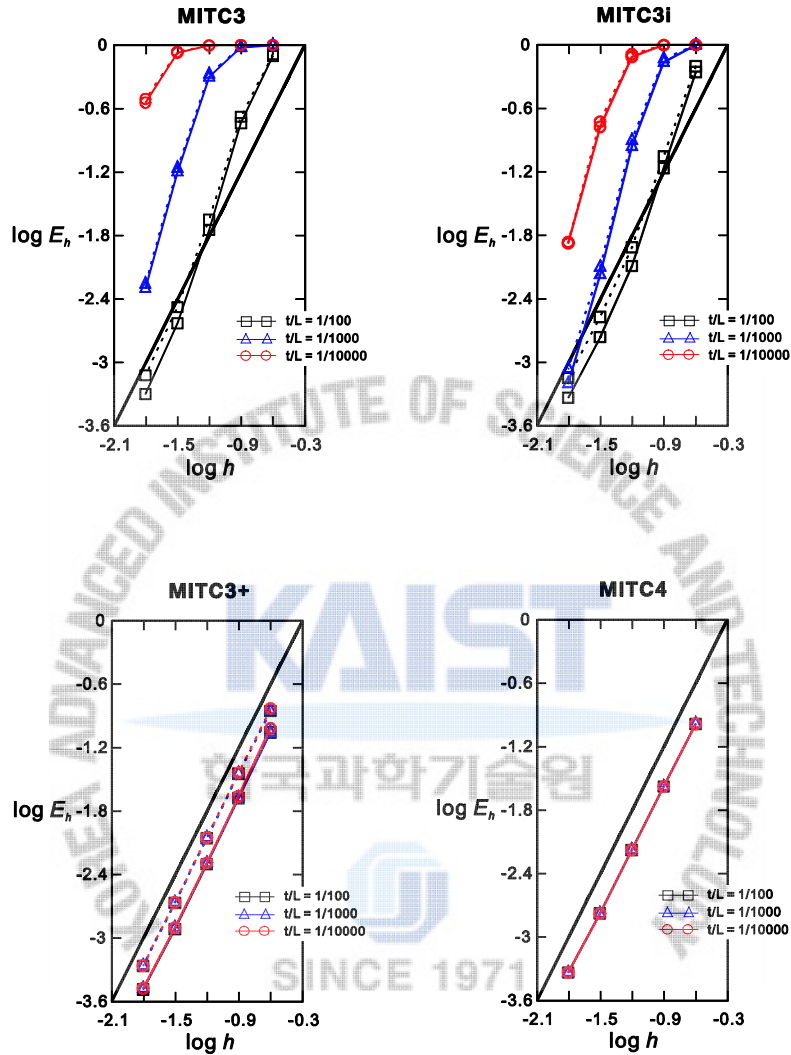


Fig. 4.5 Convergence curves for the fully clamped square plate problem. The bold line represents the optimal convergence rate. The solid and dotted lines correspond to the results obtained by the mesh patterns in Figs. 3.12(a) and (b), respectively.

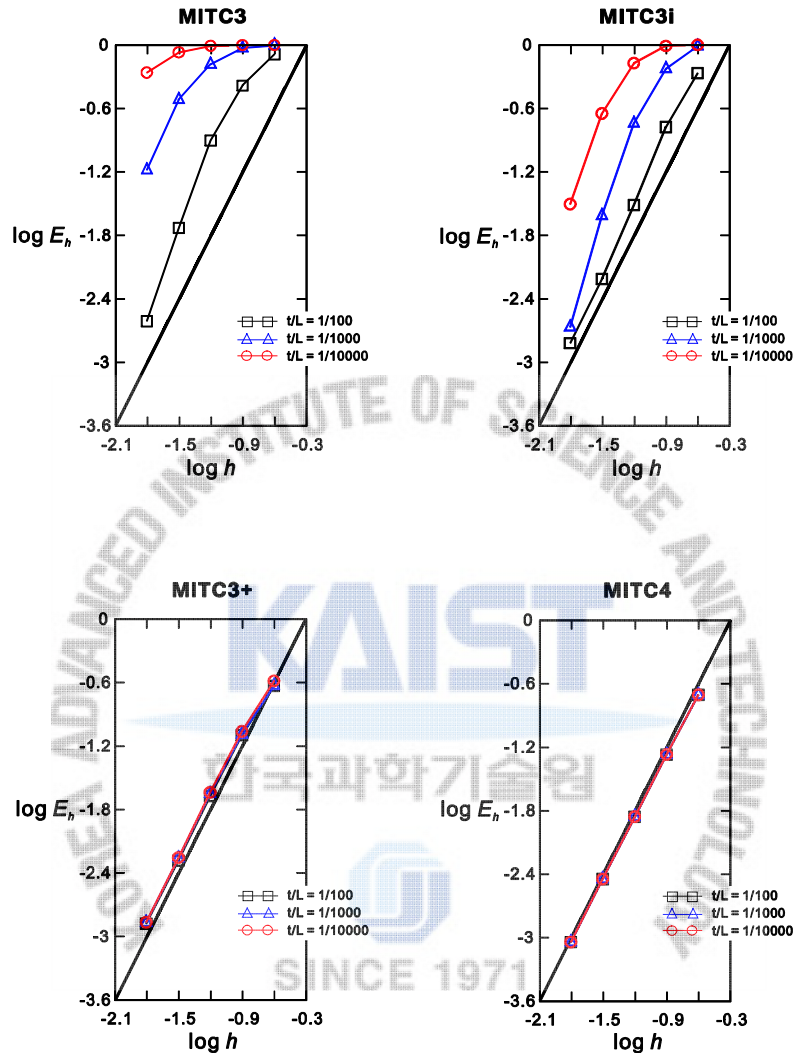


Fig. 4.6 Convergence curves for the fully clamped square plate problem with the distorted meshes shown in Fig. 3.14. The bold line represents the optimal convergence rate.

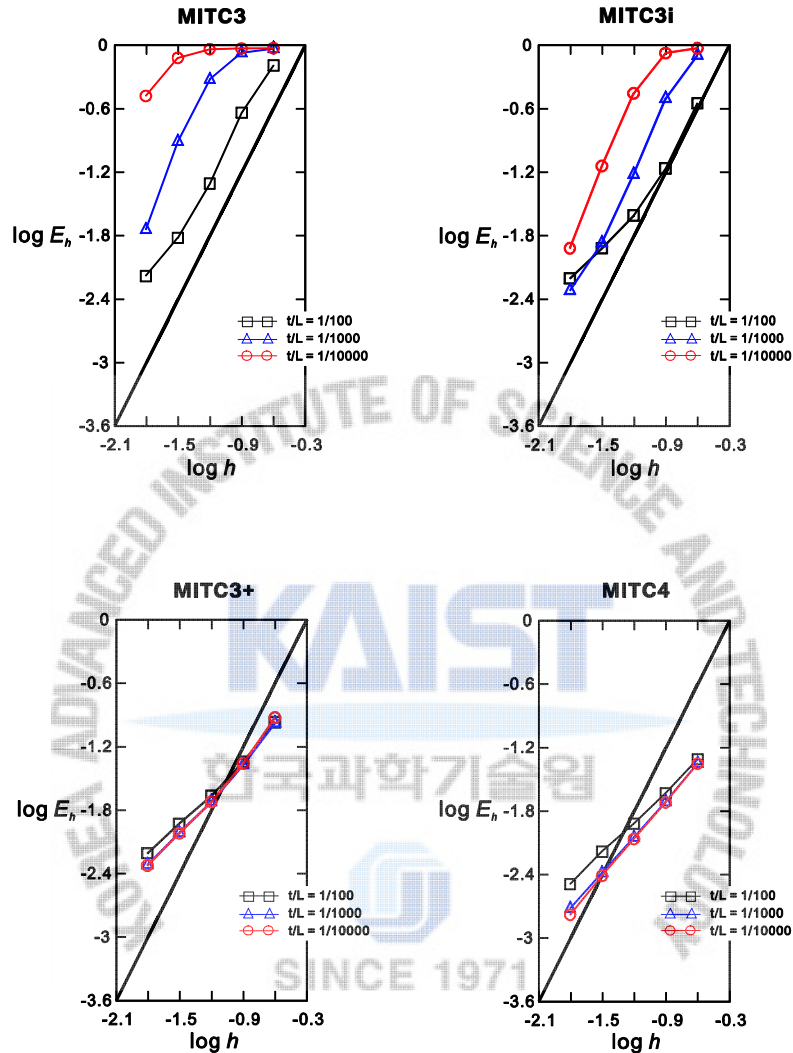


Fig. 4.7 Convergence curves for the simply supported sixty-degree skew plate problem. The bold line represents the optimal convergence rate.

The convergence behavior of the MITC3, MITC3i, MITC3+ and MITC4 shell elements is shown in Fig. 4.7. The reference solutions are obtained using a  $128 \times 128$  element mesh of MITC9 shell elements. The solutions of the triangular shell elements are calculated using  $N \times N$  element meshes ( $N = 8, 16, 32, 64$  and  $128$ ). The element size is  $h = 2L/N$ . The performance of the MITC3+ shell element is much better than those of the other triangular shell elements. The MITC3+ shell element present similar excellent convergence behavior like the MITC4 shell element.

#### 4.4.3 Cylindrical shell problems

The cylindrical shell of length  $2L$ , radius  $R$  and uniform thickness  $t$  is considered as shown in Fig. 3.18. The loading is a smoothly varying pressure  $p(\theta)$

$$p(\theta) = p_0 \cos(2\theta). \quad (4.13)$$

This shell structure shows different asymptotic behaviors depending on the boundary conditions at its ends. When both ends are free, a bending dominated problem is solved, whereas when both ends are clamped, a membrane dominated problem is considered.

Using symmetry, only the region ABCD in Fig. 3.18 is modeled. To have the membrane dominated problem, the clamped boundary condition is imposed:  $u_x = \beta = 0$  along BC,  $u_y = \alpha = 0$  along DC,  $u_z = \alpha = 0$  along AB, and  $u_x = u_y = u_z = \alpha = \beta = 0$  along AD. To have the bending dominated problem, the free boundary condition is imposed:  $u_x = \beta = 0$  along BC,  $u_y = \alpha = 0$  along DC, and  $u_z = \alpha = 0$  along AB.

Figs. 4.8 and 4.9 give the convergence curves of the MITC3, MITC3i, MITC3+ and MITC4 shell elements for the clamped and free cylindrical shell problems. The reference solutions are calculated using a  $96 \times 96$  element mesh of MITC9 shell elements. The solutions using the MITC3, MITC3i and MITC3+ and MITC4 shell elements are obtained with  $N \times N$  element meshes ( $N = 4, 8, 16, 32$ , and  $64$ ). The element size is  $h = L/N$ . In these problem solutions, the MITC3, MITC3i and MITC3+and MITC4 shell elements present similarly good convergence behaviors.

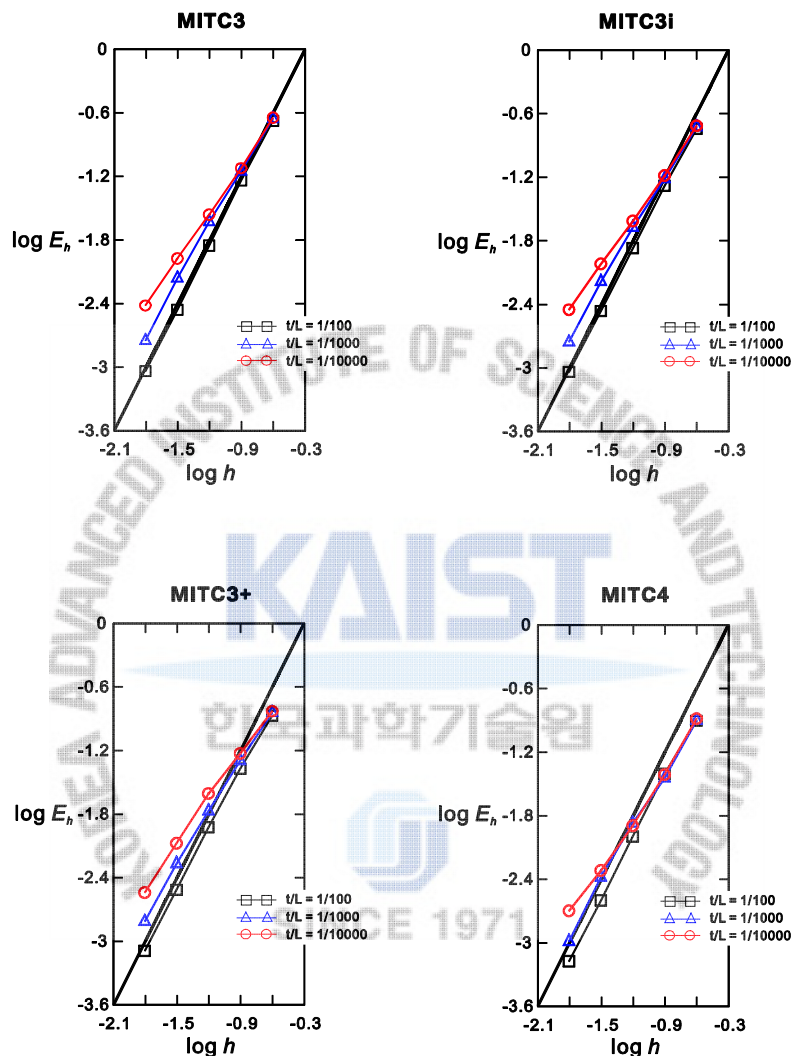


Fig. 4.8 Convergence curves for the clamped cylindrical shell problem. The bold line represents the optimal convergence rate.

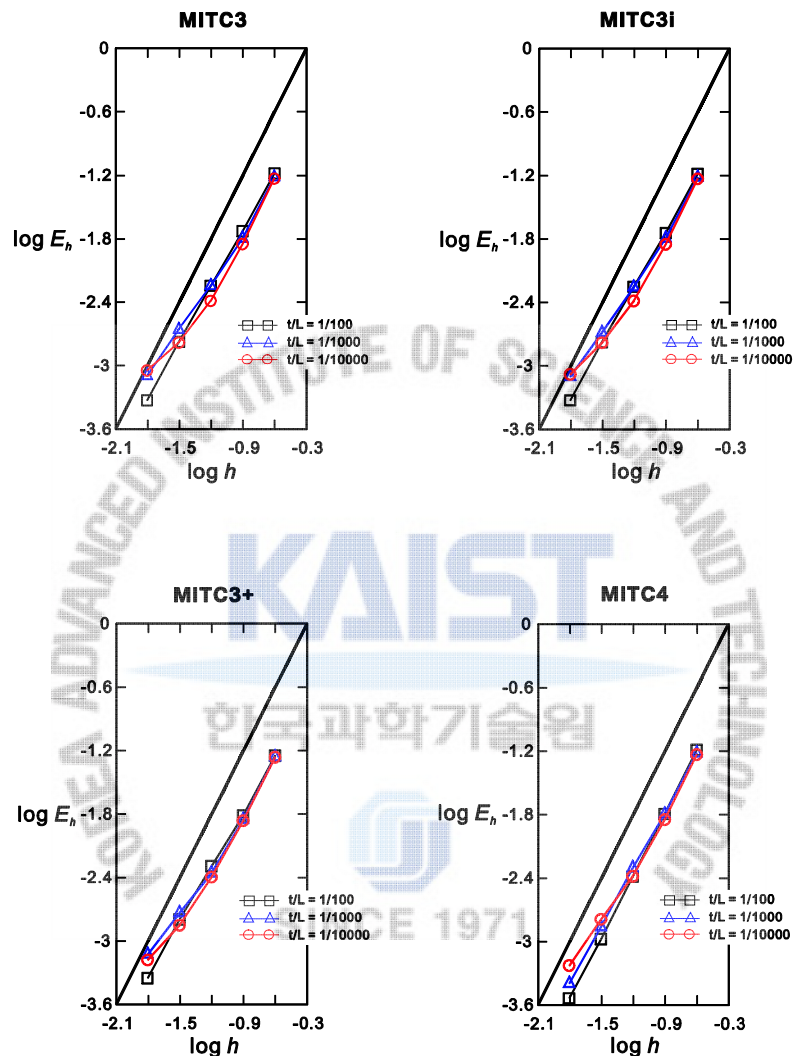


Fig. 4.9 Convergence curves for the free cylindrical shell problem. The bold line represents the optimal convergence rate.

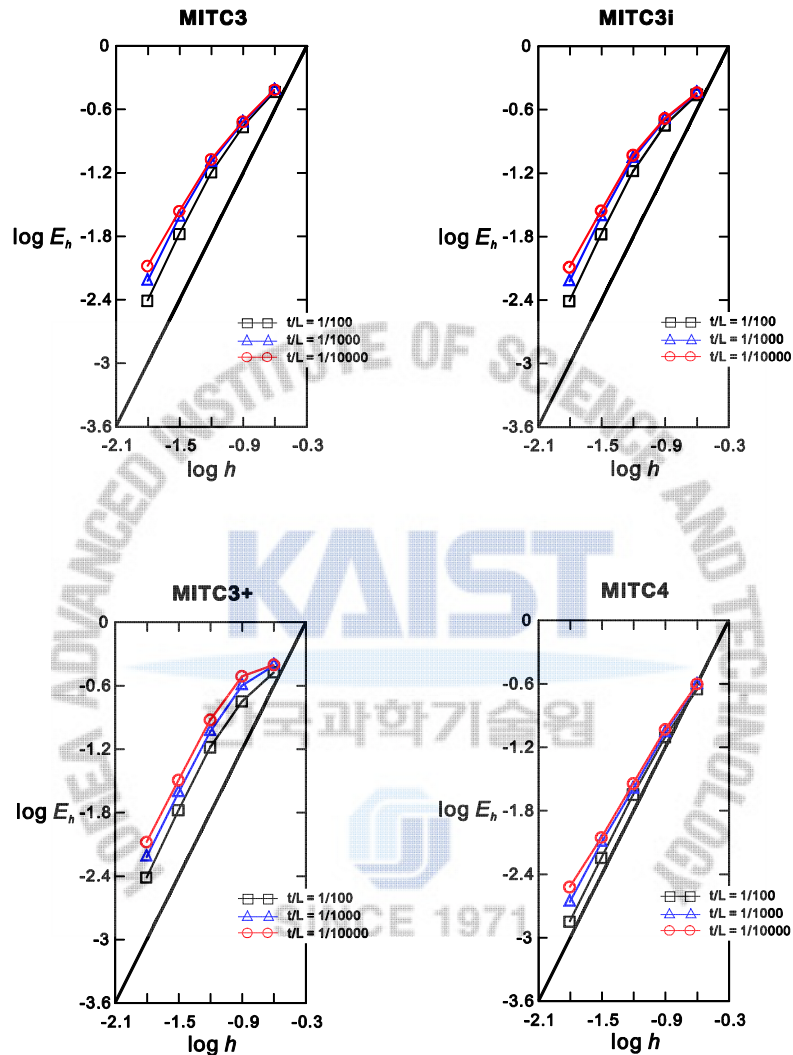


Fig. 4.10 Convergence curves for the clamped cylindrical shell problem with the distorted meshes shown in Fig. 3.14. The bold line represents the optimal convergence rate.

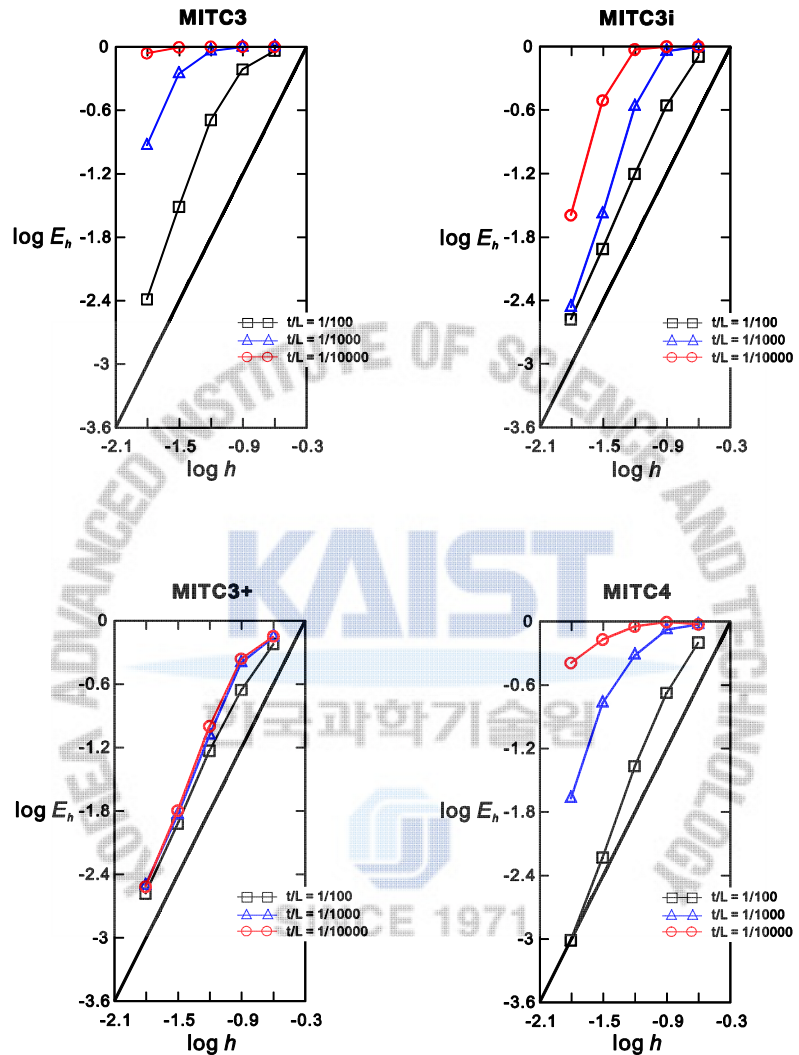


Fig. 4.11 Convergence curves for the free cylindrical shell problem with the distorted meshes shown in Fig. 3.14. The bold line represents the optimal convergence rate.

Figs. 4.10 and 4.11 give the convergence curves of the MITC3, MITC3i, MITC3+ and MITC4 shell elements when the distorted meshes in Fig. 3.14 are used. In the membrane dominated problem, all four shell elements show similarly good convergence behavior. In the bending dominated problem, in particular, even though the convergence behavior of the MITC4 shell element deteriorates due to locking, the MITC3+ shell element still shows a good performance.

#### 4.4.4 Hyperboloid shell problems

Finally, the hyperboloid shell shown in Fig. 3.23 is considered. The mid-surface of the shell structure is given by

$$x^2 + z^2 = 1 + y^2; \quad y \in [-1, 1]. \quad (4.14)$$

As for the cylindrical shell problems, a smoothly varying pressure is applied, see Fig. 3.18,

$$p(\theta) = p_0 \cos(2\theta). \quad (4.15)$$

A bending dominated behavior is obtained with free ends and a membrane dominated behavior is given with clamped ends. The bending dominated problem is known to be difficult to solve accurately [2].

Due to symmetry, the analyses are performed using one-eighth of the structure corresponding to the shaded region ABCD in Fig. 3.23(a). For the membrane dominated case, the clamped boundary condition is imposed:  $u_z = \beta = 0$  along BC,  $u_x = \beta = 0$  along AD, and  $u_y = \alpha = 0$  along DC, and  $u_x = u_y = u_z = \alpha = \beta = 0$  along AB. For the bending dominated case, the free boundary condition is imposed:  $u_z = \beta = 0$  along BC,  $u_x = \beta = 0$  along AD, and  $u_y = \alpha = 0$  along DC.

In both cases, a  $96 \times 96$  element mesh of MITC9 shell elements is used to obtain the reference solutions. The solutions of the MITC3, MITC3i and MITC3+ shell elements are calculated using  $N \times N$  element meshes ( $N = 4, 8, 16, 32$  and  $64$ ). The element size is  $h = L/N$ . In the clamped hyperboloid shell case, a boundary layer of width  $6\sqrt{t}$  is considered for half of the mesh, see Fig. 3.23(b). In the free hyperboloid shell case, the thin boundary layer is not specially considered [2].

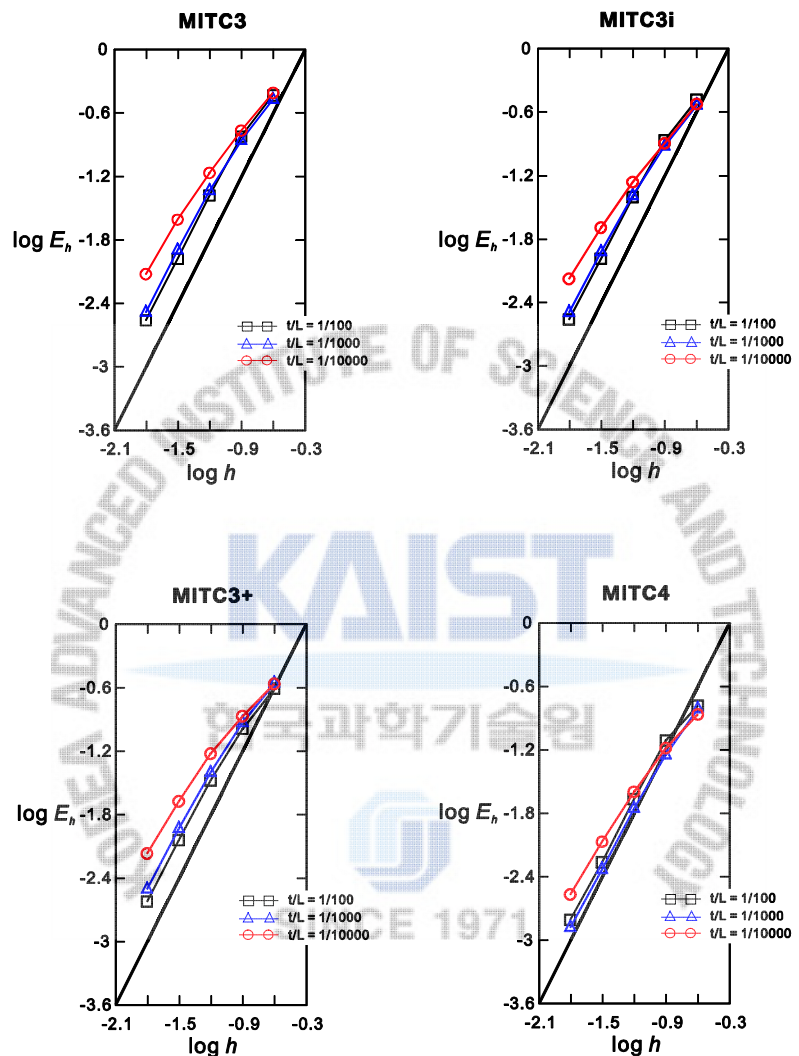


Fig. 4.12 Convergence curves for the clamped hyperboloid shell problem. The bold line represents the optimal convergence rate.